

# High-Entropy Alloys for Cathode, Electrolyte, and Anode Applications in Lithium–O<sub>2</sub> Batteries

Xin Xu, Wanzhen Li, Wentao Wang, Ningxuan Zhu, Chuan Tan,\* Xiangwen Gao,\* and Yuhui Chen\*

Lithium–oxygen (Li–O<sub>2</sub>) batteries have attracted substantial interest due to their high theoretical specific energy and environmental benignity. However, their practical electrochemical performance remains hampered by sluggish cathode reaction kinetics, unstable solid electrolyte interphase (SEI) at electrode/electrolyte interfaces, and lithium dendrite growth. Addressing these system-wide challenges necessitates the development of novel functional materials as a pivotal strategy. Among explored materials, high-entropy alloys (HEAs) demonstrate significant advantages

through finely tunable composition and electronic structure, enabling synergistic functionality that offers new pathways for enhancing the comprehensive performance of Li–O<sub>2</sub> batteries. This review outlines the fundamental reaction mechanisms and core challenges of Li–O<sub>2</sub> batteries, and then systematically examines recent advances in HEA applications across three critical domains: cathode catalyst design, electrolyte optimization, and anode protection. Finally, perspectives on future research directions for HEAs in Li–O<sub>2</sub> batteries are offered.

## 1. Introduction

Lithium–oxygen (Li–O<sub>2</sub>) batteries, as a pivotal next-generation energy storage technology, exhibit disruptive application potential in electric vehicles and portable electronics owing to their ultrahigh theoretical energy density of 3500 Wh kg<sup>-1</sup>.<sup>[1–9]</sup> The battery operates through reversible electrochemical reactions between lithium metal and oxygen, enabling efficient energy storage and release. With the accelerating global transition toward clean and low-carbon energy structures, Li–O<sub>2</sub> battery research has emerged as a critical pathway for overcoming current energy storage limitations and achieving carbon neutrality goals.<sup>[10–14]</sup> However, practical deployment faces severe and interconnected interfacial challenges. At the cathode, sluggish oxygen reduction/evolution reaction (ORR/OER) kinetics cause rapid efficiency decay, while pore clogging by lithium peroxide (Li<sub>2</sub>O<sub>2</sub>) discharge products obstructs oxygen transport.<sup>[15]</sup> The electrolyte undergoes continuous decomposition through parasitic reactions with lithium metal, increasing interfacial resistance.<sup>[15–19]</sup> At the anode, uneven lithium deposition leads to dendritic growth, posing serious safety hazards such as short circuits, alongside rapid

capacity fade due to severe cycling-induced volume changes that compromise electrode integrity.<sup>[20–27]</sup> These multifaceted interfacial issues across cathode, electrolyte, and anode critically constrain the energy efficiency, cycle life, and safety reliability of Li–O<sub>2</sub> batteries.

Over the past decade, researchers have pursued sustained exploration into optimizing individual battery components to address these challenges, including cathodic catalytic activity enhancement, electrolyte stability broadening, and lithium metal anode protection.<sup>[28]</sup> However, these efforts frequently encounter significant mutual constraints among component functionalities. For example, enhancing cathodic catalytic activity may compromise structural stability, while electrolytes with broadened electrochemical windows often intensify interfacial side reactions with active species.<sup>[28,29]</sup> Furthermore, reinforced anode protection strategies typically impair ionic conductivity. Compiling these competing requirements remains challenging given the inherent compositional constraints of conventional material systems. Consequently, progress toward simultaneously achieving critical objectives, including high energy density, extended cycle life, and stable interfaces, has been limited, with persistent technological obstacles preventing decisive breakthroughs.

Recent years have witnessed the emergence of high-entropy materials as a promising pathway to overcome these challenges,<sup>[30–33]</sup> leveraging synergistic contributions from four fundamental effects that enable novel material systems combining tunable functionality with thermodynamic stability.<sup>[34–39]</sup> The high-entropy impact originates from the high atomic disorder of multiprincipal elements, favoring the formation of stable solid-solution phases that confer exceptional thermal stability and mechanical properties.<sup>[40–45]</sup> Lattice distortion effects from atomic size mismatch induce severe lattice strain, significantly enhancing strength, hardness, and deformation resistance while modifying electronic structures.<sup>[46–51]</sup> Diffusion sluggishness, stemming from

X. Xu, W. Li, W. Wang, N. Zhu, Y. Chen  
State Key Laboratory of Materials-Oriented Chemical Engineering  
College of Chemical Engineering  
Nanjing Tech University  
Nanjing, Jiangsu 211816, China  
E-mail: cheny@njtech.edu.cn

C. Tan, X. Gao  
Research Center  
Global Institute of Future Technology  
Shanghai Jiao Tong University  
Shanghai 200240, China  
E-mail: tanchuantc@sjtu.edu.cn  
xiangwen.gao@sjtu.edu.cn

impeded diffusion pathways and elevated activation energies, substantially inhibits elemental migration to enhance structural stability and oxidation/corrosion resistance.<sup>[52–58]</sup> The cocktail effect arises from complex elemental interactions, yielding bulk properties surpassing linear combinations of individual components to create unique functionalities. Atomic-level intermixing of multiple principal elements circumvents the rigid stoichiometric limitations inherent to conventional materials, enabling structural tunability and creating new pathways for performance optimization.<sup>[59–61]</sup> These intrinsic attributes position high-entropy systems to simultaneously overcome critical bottlenecks in Li–O<sub>2</sub> batteries (Figure 1), including cathodic catalytic efficiency, electrolyte stability, and anodic interface compatibility, while establishing a fundamental theoretical framework for synergistic multi-component evolution.<sup>[61]</sup>

In this review, we systematically examine the multifaceted applications of high-entropy materials in Li–O<sub>2</sub> batteries. This comprehensive examination focuses on three critical domains: 1) cathode electrocatalyst design, exploring electronic structure modulation strategies in high-entropy alloys (HEAs) and their enhancement mechanisms for ORR/OER kinetics; 2) high-entropy

electrolyte (HEE) engineering, elucidating chemical principles and dynamic evolution laws governing multicomponent synergistic interface stabilization; and 3) anode protection strategies, summarizing physicochemical modulation approaches that employ high-entropy materials to suppress lithium dendrite growth. Finally, we outline future challenges and interdisciplinary research directions, including machine learning-guided composition optimization and operando interfacial characterization techniques. This framework provides theoretical foundations and technical references for designing next-generation high-energy-density batteries.

## 2. Brief Overview of Li–O<sub>2</sub> Batteries and High-Entropy Catalysts

### 2.1. The Reaction Mechanism of Li–O<sub>2</sub> Batteries

The reaction in Li–O<sub>2</sub> batteries constitutes a complex electrochemical process occurring at the solid (electrode)–liquid (electrolyte)–gas (O<sub>2</sub>) triple-phase interface.<sup>[62–65]</sup> During discharge,



**Xin Xu** obtained his bachelor's in applied chemistry from Chaohu University in 2024. Currently, he works as a graduate student at Nanjing Tech University and mainly engages in lithium-air batteries.



**Wanzen Li** received his B.S. in chemistry from Chongqing University of Arts and Sciences. Currently, she works as a graduate student at Nanjing Tech University and mainly engages in lithium-air batteries.



**Wentao Wang** received his B.S. degree from Nanjing Tech University. He is a PhD student at Nanjing Tech University, and his main research direction is in-situ mass spectrometry studies of lithium-ion batteries.



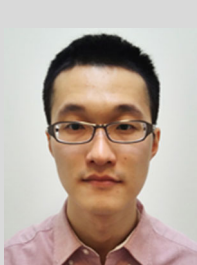
**Ningxuan Zhu** obtained his Bachelor's degree from Nanjing Tech University. He is a PhD student at Nanjing Tech University, and his main research direction is metal-air batteries.



**Chuan Tan** obtained his Ph.D. from Nanjing Tech University. Later, he engaged in postdoctoral research at Shanghai Jiao Tong University. His main research direction is metal-air batteries.



**Xiangwen Gao** Prof. Xiangwen Gao obtained his Ph.D. from the University of St Andrews in 2018. Later, he engaged in postdoctoral research at the University of Texas at Austin from 2019 to 2020 and the University of Oxford from 2020 to 2022, and joined Shanghai Jiao Tong University in 2023. His research interests include new electrochemical energy storage technology systems such as lithium-air and solid-state lithium metal batteries.



**Yuhui Chen** Prof. Yuhui Chen obtained his Ph.D. from the University of St Andrews in 2014. Later, he worked with Prof. Peter Bruce at the University of Oxford on metal-air batteries. In 2017, he joined Nanjing Tech University. His research interests include electrochemical catalysis and novel batteries such as metal-air batteries.

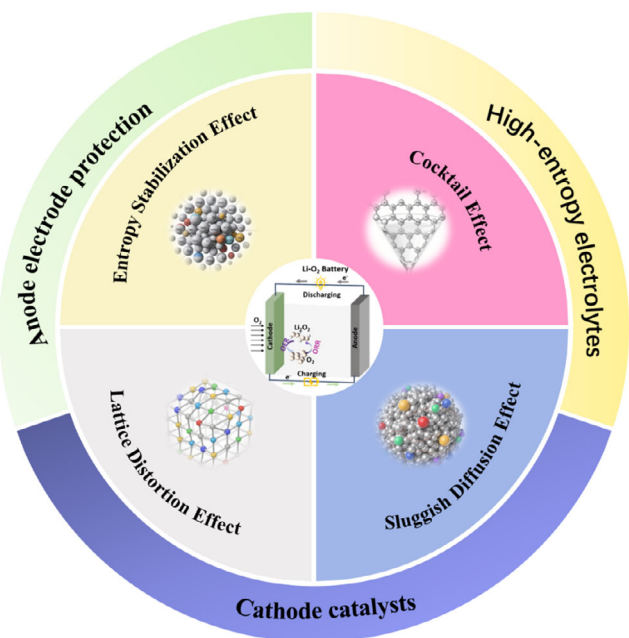


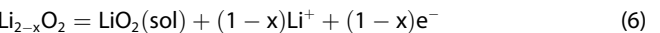
Figure 1. Schematic diagram of the structure of this review.

metallic lithium at the anode loses electrons to form  $\text{Li}^+$  ions, which diffuse into the electrolyte. At the cathode,  $\text{O}_2$  acquires electrons through the external circuit to form superoxide ions ( $\text{O}_2^-$ ) (Equation 1), followed by the combination of  $\text{O}_2^-$  with  $\text{Li}^+$  to generate the intermediate product  $\text{LiO}_2$  (Equation 2). The formation pathway of  $\text{Li}_2\text{O}_2$ —solution-mediated versus surface-mediated—depends on the location of  $\text{LiO}_2$  generation, which is determined by whether  $\text{LiO}_2$  adsorbs onto the electrode surface or dissolves into the electrolyte.<sup>[62]</sup> Multiple factors, including electrolyte solvent properties, electrode surface adsorption strength, electrode potential, and discharge current, govern this distribution. When  $\text{LiO}_2$  adsorbs onto the electrode surface, it undergoes further electrochemical oxidation to form film-like  $\text{Li}_2\text{O}_2$  (Equation 3). Conversely, when dissolved in the electrolyte,  $\text{LiO}_2$  undergoes a disproportionation reaction to generate larger toroidal  $\text{Li}_2\text{O}_2$  particles (Equation 4).



During the charging process,  $\text{Li}_2\text{O}_2$  undergoes decomposition. However, the insulating nature of  $\text{Li}_2\text{O}_2$ , characterized by its wide bandgap of  $\approx 4\text{--}5$  eV, necessitates significant charging overpotential for decomposition.<sup>[66,67]</sup> This process initiates through partial delithiation of  $\text{Li}_2\text{O}_2$ , forming  $\text{Li}_{2-x}\text{O}_2$  (Equation 5). Subsequent reaction mechanisms mirror the reverse of discharge pathways, similarly differentiating between solution- and surface-mediated

routes: In the solution-mediated pathway,  $\text{Li}_{2-x}\text{O}_2$  decomposes into dissolved  $\text{LiO}_2$  (sol) (Equation 6), which then undergoes disproportionation to regenerate  $\text{Li}_2\text{O}_2$  and  $\text{O}_2$  (Equation 4). Conversely, in the surface-mediated pathway,  $\text{Li}_{2-x}\text{O}_2$  directly decomposes into  $\text{O}_2$  and  $\text{Li}^+$  (Equation 7).



## 2.2. Challenges of Rechargeable $\text{Li}-\text{O}_2$ Batteries

The central bottleneck impeding efficient energy conversion in  $\text{Li}-\text{O}_2$  batteries lies in their sluggish kinetics for the ORR and OER.<sup>[66,67]</sup> The high energy barriers and complex reaction mechanisms inherent in the ORR process result in a discharge voltage significantly below the theoretical value (2.96 V vs  $\text{Li}^+/\text{Li}$ ), substantially reducing energy efficiency.<sup>[68]</sup> In contrast, the slow kinetics of the oxygen evolution reaction predominantly drive the significant charging voltage increase beyond theoretical values. This kinetic hysteresis directly induces substantial voltage overpotential during charge/discharge cycles, constituting the fundamental cause of the battery's low energy efficiency and limited rate capability. Consequently, developing highly efficient catalyst systems to reduce the activation energy barriers for ORR/OER and accelerate reaction rates represents a pivotal step toward overcoming the kinetic limitations of  $\text{Li}-\text{O}_2$  batteries and advancing their practical implementation.<sup>[69]</sup>

Noble metal and transition metal oxide (TMO) catalysts are commonly employed in  $\text{Li}-\text{O}_2$  batteries.<sup>[70–72]</sup> They synergistically accelerate ORR and OER kinetics by providing active sites on electrode surfaces to facilitate the adsorption/activation of reactants ( $\text{O}_2, \text{Li}^+$ ), stabilize reaction intermediates, and regulate the nucleation/growth/decomposition behavior of  $\text{Li}_2\text{O}_2$ .<sup>[73]</sup> The catalytic potential of various noble metals has been experimentally verified. Yang et al. demonstrated that Au and Pt nanoparticles enhance battery round-trip efficiency.<sup>[74]</sup> Gasteiger et al. systematically evaluated the ORR activities of polycrystalline Pd, Pt, Ru, and Au, establishing the activity order as  $\text{Pd} > \text{Pt} > \text{Ru} \approx \text{Au} > \text{GC}$ , with Pd exhibiting superior ORR catalytic performance.<sup>[75]</sup> Wang et al. achieved a high capacity of 9800 mAh g<sup>-1</sup>, 150 cycles, and a low overpotential of 0.37 V using Ru nanocrystals supported on carbon black.<sup>[76]</sup> Regarding TMOs, Bethune et al. revealed that cathodes incorporating TMOs (e.g.,  $\text{RuO}_2$ ) maintain OER efficiencies comparable to carbon electrodes (69% vs 73%) while simultaneously reducing overpotentials (e.g., 400 mV decrease for  $\text{RuO}_2$ ) and mitigating passivation/electrolyte decomposition.<sup>[77]</sup>

Despite their ability to reduce overpotentials in  $\text{Li}-\text{O}_2$  batteries, conventional catalysts such as noble metals and TMOs still face critical challenges. While noble metals exhibit favorable ORR activity, they inadequately catalyze  $\text{Li}_2\text{O}_2$  decomposition and significantly promote side reactions, inevitably leading to

byproduct accumulation during cycling.<sup>[78]</sup> Additionally, their high cost impedes scalable implementation. TMOs, conversely, generally demonstrate limited catalytic performance.<sup>[77]</sup> An ideal catalyst for Li–O<sub>2</sub> batteries must possess bifunctional characteristics: efficiently catalyzing ORR to inhibit side reactions and enable high-capacity discharge while simultaneously addressing sluggish cathode kinetics by effectively catalyzing Li<sub>2</sub>O<sub>2</sub> decomposition, thereby ensuring superior cycling stability. Current catalyst systems fail to meet these requirements, underscoring the need to develop novel catalyst systems.

### 2.3. Application of High-Entropy Catalysts in Li–O<sub>2</sub> Batteries

HEAs demonstrate significant potential in electrocatalysis due to their ability to overcome traditional catalytic limitations through tunable *d*-band centers for optimized adsorption energetics, lattice distortion-induced active sites for enhanced kinetics, and entropic stabilization for operational durability. This multifunctional synergy enables superior bifunctional catalytic activity for ORR and OER in Li–O<sub>2</sub> batteries (Table 1). Guo et al. engineered a six-component HEAs catalyst system comprising HEA, HEA-Ir, HEA-Pt, HEA-PtIr, and PtIr variants, with Fe/Co/Ni/Mn as the base. The high-entropy strategy enabled continuous *d*-band center tuning, yielding the sequence (Figure 2a): HEA > PtIr > HEA-PtIr > HEA-Ir > HEA-Pt. Differential electrochemical mass spectrometry (DEMS) analysis (Figure 2b) confirmed efficient bifunctionality with near-ideal electron/O<sub>2</sub> ratios (ORR: 1.94 e<sup>−</sup>/O<sub>2</sub>; OER: 2.02 e<sup>−</sup>/O<sub>2</sub>). Li–O<sub>2</sub> batteries with six-component HEA-PtIr exhibited the lowest overpotential (0.38 V) while maintaining stability over 2000 h cycling (at 4000 mAh g<sup>−1</sup> limited capacity). Full discharge capacity reached 39.1 Ah g<sup>−1</sup>, demonstrating rapid reaction kinetics, high capacity, and exceptional cycling stability (Figure 2c).<sup>[79]</sup> While HEAs' remarkable performance originates from intrinsic properties and multmetallic interactions, the current reliance on precious metals (Pd, Ru, Co, Ir, Au, Ag, Pt) necessitates future exploration of cost-effective alternative elements.

To address the high-cost limitations of HEAs, researchers have integrated the electronically tunable perovskite structure with

high-entropy strategies, developing high-entropy perovskite oxides (HEPOs). Zhang et al. reported the synthesis of HEPO and Ru@HEPO catalysts. When employed as cathodes in Li–O<sub>2</sub> batteries, Ru@HEPO exhibited discharge/charge capacities of 12,275/11882 mAh g<sup>−1</sup> at 50 mA g<sup>−1</sup> with a low overpotential of 0.65 V (Figure 2d,e). At a fixed capacity of 1000 mAh g<sup>−1</sup> under 300 mA g<sup>−1</sup> current density, it demonstrated superior cyclability (345 cycles) compared to HEPO (260 cycles, 0.81 V overpotential). Ex situ X-ray photoelectron spectroscopy (XPS) and Charge Transfer Resistance (RCT) analyses confirmed Ru@HEPO's effective catalytic decomposition of Li<sub>2</sub>O<sub>2</sub>, validating its bifunctional capability. Through computational analysis of adsorption energies and Gibbs free energies for reaction intermediates, the researchers revealed HEPO's weak adsorption of LiO<sub>2</sub> intermediates, favoring solution-mediated growth of bulk Li<sub>2</sub>O<sub>2</sub> during discharge. This process consequently increases interface resistance between discharge products and HEPO.<sup>[80]</sup> Complementing this, Shu et al. designed LaSr(STM)O<sub>3</sub> via strain engineering to enhance LiO<sub>2</sub> intermediate adsorption by modulating Co<sup>3+</sup> 3*d*-orbital configurations, introducing Ni-induced lattice compressive strain, shortening Co–O bonds, and modifying 3*d*-orbital occupation to upshift the Co *d*-band center. Density functional theory (DFT) calculations confirmed this strategy effectively mitigated HEPOs inherent weak LiO<sub>2</sub> adsorption (Figure 2f). The LaSr(STM)O<sub>3</sub> catalyst delivered exceptional performance: a high discharge capacity of 19,133.6 mAh g<sup>−1</sup>, extended cycling stability (226 cycles), and a reduced overpotential of 0.79 V. In situ DEMS further demonstrated reversible Li<sub>2</sub>O<sub>2</sub> conversion, with near-ideal O<sub>2</sub> consumption/release ratios of 2e<sup>−</sup>/O<sub>2</sub> during discharge/charge processes.<sup>[81]</sup>

Beyond optimizing ORR/OER performance through high-entropy strategies and strain engineering to modulate intrinsic electronic structures, dimensional engineering of catalyst architectures demonstrates significant advantages. Constructing nanoscale high-entropy catalysts across 0D to 3D frameworks substantially increases specific surface areas and maximizes active site exposure, thereby synergistically enhancing interfacial reactivity.

**Table 1.** Summary of electrochemical performance with different types of high-entropy catalysts in lithium–oxygen batteries.

Catalyst	Overpotential	Discharge capacity [mAh g <sup>−1</sup> ]	Current density [mA g <sup>−1</sup> ]	Cycling performance [mAh g <sup>−1</sup> ]	Ref.
HEAPtIr	0.38 V	39,100	200	150 cycles at a specific capacity of 1000	[79]
HEA@Pt–Pt <sub>SAS</sub>	0.3 V	13,116	1000	470 cycles at a specific capacity of 1000	[124]
Ru@HEPO	0.65 V	12,275	300	345 cycles at a specific capacity of 1000	[80]
HEO-PMA SNWs	—	11,206	100	213 cycles at a specific capacity of 500	[83]
LaSr(STM)O <sub>3</sub>	0.79 V	19,133	200	226 cycles at a specific capacity of 1000	[81]
HESe	0.37 V (ORR) 1.27 V (OER)	3650	500	480 cycles at a specific capacity of 500	[125]
(CoFeNiMnCu) <sub>9</sub> S <sub>8</sub>	1.25 V	15,100	200	115 cycles at a specific capacity of 1000	[126]
KCoMnNiMgZnF <sub>3</sub> -HEC	0.24 V (ORR) 0.46 V (OER)	22,104	1000	500 cycles at a specific capacity of 1000	[127]
CuCoNiZnAl-T-NaOH HEOS	1.68 V	12,049	200	250 cycles at a specific capacity of 500	[128]
HEA-PtPdIrRuAuAg SNR	0.87 V (OER)	5252	500	100 cycles at a specific capacity of 1000	[84]
LB-HEO	0.97 V (OER)	≈2000	100	135 cycles at a specific capacity of 1000	[129]

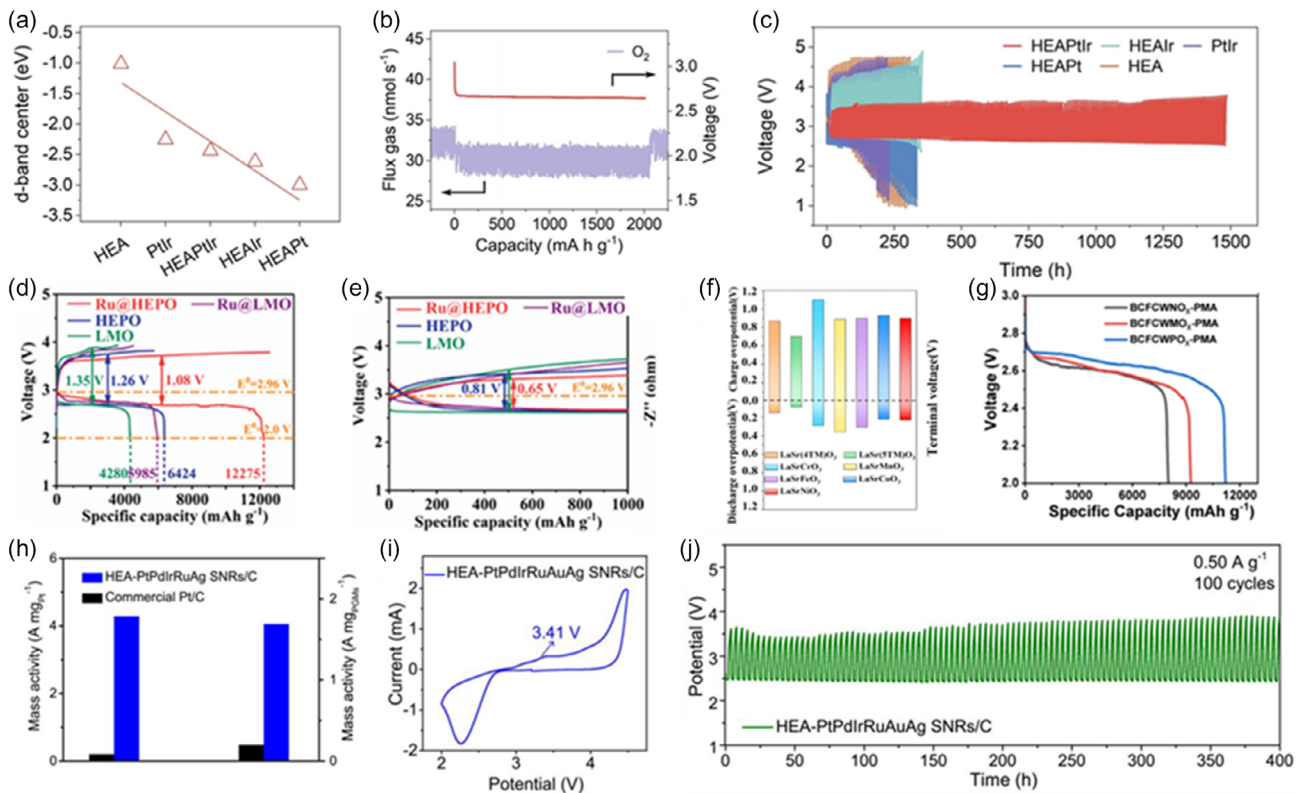


**Figure 2.** a) The *d*-band center sequence of HEA, PtIr, HEAPtIr, HEAlr, and HEAPt. b) In situ DEMS curves of the HEAPtIr cathode under LOB conditions with a rated capacity of 2000 mAh g<sup>-1</sup> and a current density of 1000 mA g<sup>-1</sup>. c) Cycling curves of lithium–oxygen batteries using different HEA materials as catalysts under conditions of 200 and 1000 mAh g<sup>-1</sup>. Reproduced with permission.<sup>[79]</sup> Copyright 2023, Wiley-VCH GmbH. Different HEPPO and LMO electrodes: d) full discharge–full charge curves at a current density of 50 mA g<sup>-1</sup>. e) Charge–discharge curves at a current density of 100 mA g<sup>-1</sup> and a rated capacity of 1000 mAh g<sup>-1</sup>. Reproduced with permission.<sup>[80]</sup> Copyright 2024, Wiley-VCH GmbH. f) Overpotential of LaSr(4TM)O<sub>3</sub>, LaSr(5TM)O<sub>3</sub>, LaSrCrO<sub>3</sub>, LaSrMnO<sub>3</sub>, LaSrFeO<sub>3</sub>, LaSrCoO<sub>3</sub>, and LaSrNiO<sub>3</sub> electrodes at a current density of 100 mA g<sup>-1</sup>. Reproduced with permission.<sup>[81]</sup> Copyright 2024, American Chemical Society. g) Full discharge curves of three different HEO-PMA SNW-based lithium–oxygen batteries at a current density of 100 mA g<sup>-1</sup>. Reproduced with permission.<sup>[82]</sup> Copyright 2025, American Chemical Society. h) Comparison of mass activity between HEA-PtPdIrRuAg SNR/C and commercial Pt/C catalysts. HEA-PtPdIrRuAg SNR/C-based LOB: i) CV curves over a 2–4 V voltage range at a scan rate of 0.05 mV s<sup>-1</sup>. j) Cycling curves at 0.50 A g<sup>-1</sup> with a rated capacity of 1000 mAh g<sup>-1</sup>. Reproduced with permission.<sup>[84]</sup> Copyright 2022, American Chemical Society.

Xia et al. fabricated ultrasmall NiCoFePtRh nanoclusters with an average diameter of 1.68 nm—the smallest reported HEA. As HER catalysts, they delivered an exceptional mass activity of 28.3 A mg<sup>-1</sup>, exceeding commercial Pt/C and Rh/C by 40.4 and 74.5, respectively.<sup>[82]</sup> 1D electrocatalysts such as nanowires and nanotubes exhibit high aspect ratios that facilitate abundant active site accessibility and directional charge transport along the longitudinal axis. Wang and Zhang et al. synthesized a series of HEO-PMA (phosphomolybdic acid, H<sub>3</sub>PMO<sub>12</sub>O<sub>40</sub>)-stabilized nanowires (SNWs) ranging from single-component (BiO<sub>x</sub>-PMA) to hexa-component systems (BiCuFeCeWPtO<sub>x</sub>-PMA). When employed as Li–O<sub>2</sub> battery cathodes, discharge capacity increased progressively from 1651 to 11,206 mAh g<sup>-1</sup> (Figure 2g) and cycle life extended from 43 to 213 cycles with increasing metal oxide components (1–6 types), demonstrating the crucial role of entropy in tuning battery performance. The electrodes maintained stable cycling over 200 cycles under demanding fast-charging/slow-discharging conditions (1000 mA g<sup>-1</sup>/100 mAh g<sup>-1</sup>). Theoretical analyses revealed: 1) electron-rich PMA enhanced LiO<sub>2</sub> intermediate adsorption while reducing Li<sub>2</sub>O<sub>2</sub> decomposition barriers; 2) noncovalent

HEO-PMA interactions suppressed phase segregation; and 3) synergistic coupling between redox-active metals (reductive Bi/Cu and oxidative Fe/Ce) lowered ORR/OER overpotentials.<sup>[83]</sup>

2D materials, including nanosheets and nanoribbons, benefit from ultrathin layered structures that provide ultrahigh specific surface areas and high-density active sites. Guo et al. reported the synthesis of subnanometer-thick 2D HEA nanoribbons (SNRs). Utilizing Ag nanowires as templates, galvanic exchange enabled coreduction of multiple metal precursors, with subsequent core etching yielding SNRs of merely 0.8 nm thickness. Quinary HEA-PtPdIrRuAg SNRs exhibited exceptional ORR mass activity (4.28 A mg<sub>Pt</sub><sup>-1</sup>, Figure 2h), surpassing commercial Pd/C by 21.0-fold. Senary HEA-PtPdIrRuAuAg SNRs demonstrated OER capability via a characteristic oxidation peak at 3.41 V (Figure 2i), enabling Li–O<sub>2</sub> batteries with ultralow overpotential (0.49 V) and 100-cycle stability at 0.5 A g<sup>-1</sup>/1000 mAh g<sup>-1</sup> (Figure 2j).<sup>[84]</sup>

3D porous frameworks (e.g., nanodendrites, nanoflowers) leverage interconnected porosity and branched morphologies to maximize surface area and active site density.<sup>[85]</sup> For instance, Liu et al. combined HEA design with aerogel technology to fabricate HEA aerogels (HEAAs) as efficient CO<sub>2</sub>RR catalysts.<sup>[86]</sup> The

defective porous structure of HEAs provides abundant under-coordinated sites that enhance catalytic performance.

### 3. HEEs

Electrolytes are the critical medium for lithium-ion transport between electrodes in Li–O<sub>2</sub> battery systems. Conventional electrolytes exhibit several inherent limitations, including narrow electrochemical stability windows, poor thermal stability, formation of unstable solid electrolyte interphase (SEI) layers at electrode interfaces, and insufficient ionic conductivity.<sup>[87–89]</sup> Recent studies demonstrate that HEEs designed through multicomponent synergy ( $\geq 5$  constituents) can overcome these constraints. By forming high-entropy solvation structures and leveraging entropy-driven effects, HEEs significantly enhance lithium-ion conductivity, broaden electrochemical windows, promote favorable SEI formation, and improve thermal stability. This approach provides a novel solution pathway for transcending the performance bottlenecks of traditional electrolytes.

#### 3.1. High-Entropy Liquids

Conventional electrolytes offer advantages such as low cost, mature manufacturing processes, and high ionic conductivity (typically  $10^{-2}$ – $10^{-3}$  S cm<sup>-1</sup>).<sup>[90]</sup> However, common organic ester electrolytes suffer from narrow electrochemical windows (generally 4.2–4.3 V), beyond which decomposition triggers parasitic reactions.<sup>[91]</sup> They also exhibit interfacial instability with lithium anodes, forming unstable SEI layers that compromise cycling performance.<sup>[92]</sup>

The high-entropy strategy presents a practical improvement pathway by introducing multiple salts or solvent molecules to enhance solvation entropy and diversify solvation structures, thereby improving cycling stability and ionic conductivity.

Marnix Wagemaker et al. designed an entropy-driven electrolyte by blending multiple lithium salts (LiPF<sub>6</sub>, LiTFSI, LiFSI, LiDFOB, LiNO<sub>3</sub>) with a single solvent (EC/DMC) to create a multisalt HEE (1.4 M LiPF<sub>6</sub>-EDF). This formulation dramatically increased LiNO<sub>3</sub> solubility (0.1 M vs  $\leq 1000$  ppm in conventional electrolytes). The electrolyte formed an inorganic-dominated SEI (6–7 nm) on lithium metal (Figure 3a). Theoretical computations and molecular dynamics simulations reveal that HEEs performance enhancement primarily stems from weak solvation effects arising from high solvation entropy and multianion synergistic coordination (Figure 3b). Li//Cu half-cells employing HEEs exhibit exceptional coulombic efficiency exceeding 99%. These electrolytes demonstrate stable cycling at 4.3 V, with full cells composed of Li//NCM811 retaining 82% capacity after 400 cycles at 0.5 C (Figure 3c).<sup>[93]</sup> However, the high concentration (1.4 M) may induce elevated viscosity. Recent studies have explored lower concentration formulations to circumvent such viscosity constraints while retaining performance benefits. Marnix Wagemaker et al. demonstrated a comparable high-entropy liquid electrolyte strategy employing multiple lithium salts (LiTFSI, LiFSI, LiDFOB, LiNO<sub>3</sub>) in a single DME solvent. This HEEs system maintains high oxidation stability (4.51 V) even at a low salt concentration of 0.6 M. Li||LiFePO<sub>4</sub> cells achieve over 95% capacity retention after 500 cycles (comprising three cycles at 0.2 C followed by cycling at 1 C) (Figure 3d), while Li||NCM811 cells retain >80% capacity after 600 cycles at 6 C (Figure 3e). The

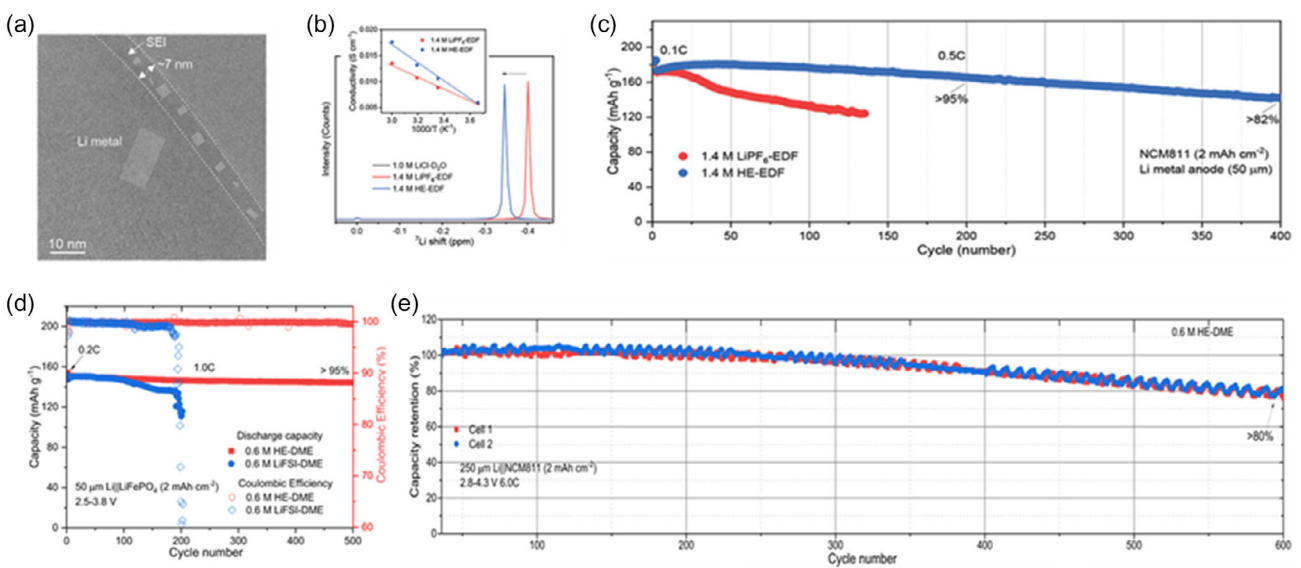


**Figure 3.** a) Cryo-transmission electron microscopy (Cryo-TEM) images showing microstructure of deposited lithium metal and interphase with 1.4 m HE-EDF electrolyte. b) Liquid  $+7\text{Li}$  NMR spectra of 1.4 m LiPF<sub>6</sub>-EDF and 1.4 m HE-EDF electrolytes. The inset shows the lithium ionic conductivity of the 1.4 m LiPF<sub>6</sub>-EDF and 1.4 m HE-EDF electrolytes at various temperatures. c) Capacity retention of Li||NCM811 cells with 1.4 m LiPF<sub>6</sub>-EDF or 1.4 m HE-EDF electrolytes cycled between 2.8 and 4.3 V with 0.1C (1.0C = 180 mA g<sup>-1</sup>) for three cycles and 0.5 C for the following cycles. The areal capacity of the NCM811 electrode is 2 mAh m<sup>-2</sup>, and the lithium-metal anode is 50  $\mu\text{m}$ . Reproduced with permission.<sup>[93]</sup> Copyright 2023, The Authors. Advanced Materials is published by Wiley-VCH GmbH. d) Li||LiFePO<sub>4</sub> (LFP) battery cycling 3 times at 0.2 C rate, followed by cycling at 1 C rate. e) Cycling curve of the NCM811 battery at a 6.0 C rate in 0.6 M HE-DME electrolyte. Reproduced with permission.<sup>[94]</sup> Copyright 2023, The Author(s), under exclusive license to Springer Nature Limited.

0.6 M concentration circumvents the high viscosity of concentrated electrolytes.<sup>[94]</sup>

Beyond multisalt formulations, HEE design can leverage solvent diversity. Cui et al. implemented a molecular diversity strategy, conceptually equivalent to HEEs, to enhance lithium metal battery performance. This approach elevates solvation entropy through increased molecular heterogeneity (multisolvent blending), reducing ion cluster size without altering solvation enthalpy. Suppressing Li<sup>+</sup>-FSI-aggregation simultaneously achieves high ionic conductivity and interfacial stability. Three electrolytes were engineered: EL2 (1M LiFSI in DME-TTE, TTE as cosolvent), EL4 (1M LiFSI in DME-DEE-DEGDME-TTE, TTE as cosolvent), and EL5 (1M LiFSI in DME-DEE-DEGDME-TTE-BTFE, TTE as cosolvent with BTFE as additional cosolvent). Experimental results demonstrate EL5 exhibits double the ionic conductivity of EL2 ( $3.57 \times 10^{-3}$  vs  $1.67 \times 10^{-3} \text{ S cm}^{-1}$ ) while maintaining cycling stability at high current density (2C,  $6.2 \text{ mA cm}^{-2}$ ). Molecular dynamics simulations and X-ray scattering reveal all formulations preserve anion-enriched primary solvation shells (3 FSI<sup>-</sup> anions and 1 solvent molecule), with ion cluster dimensions decreasing with increasing solvent diversity (EL5:  $\approx 6 \text{ Li}^+/\text{cluster}$  vs EL2:  $\approx 11 \text{ Li}^+/\text{cluster}$ ). EL5 displays higher Li<sup>+</sup> diffusivity ( $3.74 \times 10^{-6} \text{ cm}^2 \text{ s}^{-1}$ ) than EL2 ( $2.45 \times 10^{-6} \text{ cm}^2 \text{ s}^{-1}$ ), consistent with conductivity trends. In anode-free pouch cells (NMC532||Cu), EL5 maintains 70% capacity retention after 80 cycles at 2C, whereas EL2 undergoes rapid degradation. Theoretical analysis attributes the superior performance of HEEs to entropy-driven effects: Elevated entropy reduces solvation free energy, promoting ion dissociation and inhibiting large cluster formation. Smaller

clusters diminish the hydrodynamic radius, thereby enhancing diffusivity and conductivity. This improved ion transport mitigates concentration polarization and local current density heterogeneity, enabling uniform Li<sup>+</sup> deposition. This entropy-mediated strategy successfully decouples the traditional conductivity-stability trade-off, providing an innovative pathway toward practical lithium metal batteries.<sup>[95]</sup>

### 3.2. High-Entropy Solid Electrolytes

Solid-state electrolytes (SSEs), solid materials capable of conducting ions (Li<sup>+</sup>) while blocking electrons, constitute the core components of all-solid-state batteries (ASSBs). Primary SSE types include perovskite, superionic conductor (LISICON-type), and garnet structures. Perovskite SSEs like LLTO can achieve ionic conductivities of  $1 \times 10^{-3} \text{ S cm}^{-1}$  but suffer from detrimental grain boundary resistance that reduces overall conductivity. LISICON-type SSEs (primarily LiM<sub>2</sub>(PO<sub>4</sub>)<sub>3</sub>, M = Zr, Ge, Ti) offer high safety, good stability, and low cost, yet face limitations including low intrinsic conductivity and large interfacial impedance at electrode interfaces. Crystallizing in a face-centered-cubic structure, garnet-type electrolytes crystallized in a face-centered-cubic structure (general formula A<sub>3</sub>B<sub>2</sub>(XO<sub>4</sub>)<sub>3</sub>, X = Li<sup>+</sup>; specific compound Li<sub>2</sub>La<sub>3</sub>Zr<sub>2</sub>O<sub>12</sub>) have garnered significant attention due to promising properties. While the tetragonal phase exhibits a room-temperature conductivity of  $3 \times 10^{-4} \text{ S cm}^{-1}$ , the cubic phase theoretically offers conductivity two orders of magnitude higher. Current challenges center on improving the interfacial compatibility of garnet electrolytes like LLZO (including

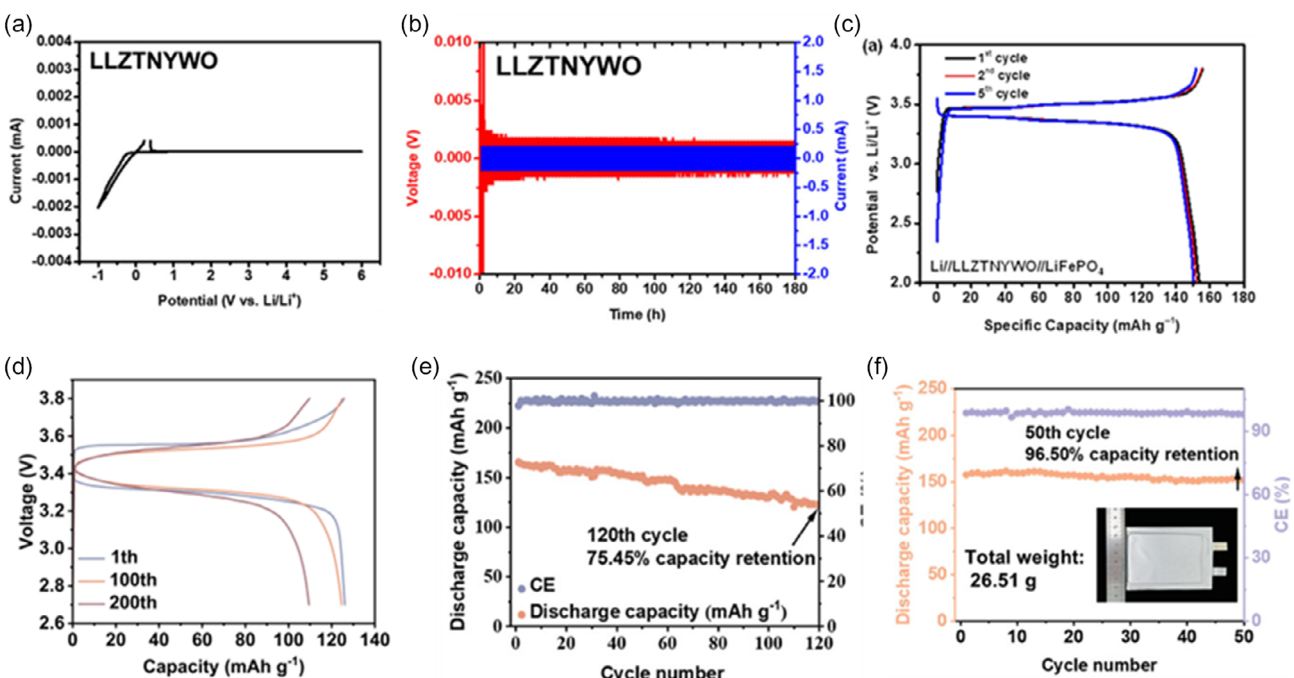


**Figure 4.** a) CV curves of batteries assembled with LLZTNYWO Li SSE at 25 °C. b) Galvanostatic cycling performance curve of Li symmetric battery assembled with LLZTNYWO electrolyte. c) Chargedischarge curves of the LFP full cell assembled with LLZTNYWO. Reproduced with permission.<sup>[98]</sup> Copyright 2022, Author(s). This article is distributed under a Creative Commons Attribution (CC BY) license. d) Chargedischarge curves of the LFP/LLNSZTO/Li battery at the 1<sup>st</sup>, 100<sup>th</sup>, and 200<sup>th</sup> cycles. e) Cycling performance curves of the solid-state battery with LFP (loading 12 mg cm<sup>-2</sup>) at 0.15 C. f) Discharge capacity and coulombic efficiency of solid-state lithium metal pouch batteries (changes over 50 cycles, with an inset showing the corresponding physical sample, dimensions: 5.5 × 8 cm). Reproduced with permission.<sup>[100]</sup> Copyright 2024, Wiley-VCH GmbH.

reactivity with atmospheric moisture and oxygen) and enhancing ionic conductivity.

The garnet structure was first identified as a novel solid lithium-ion conductor ( $\text{Li}_5\text{La}_3\text{M}_2\text{O}_{12}$ , M = Nb, Ta) by Werner J. F. Weppner. Subsequently,<sup>[96]</sup> Weppner et al. pioneered the application of  $\text{Li}_5\text{La}_3\text{Zr}_2\text{O}_{12}$  (LLZO) as an electrolyte, achieving a conductivity of  $3 \times 10^{-4} \text{ S cm}^{-1}$  at room temperature.<sup>[97]</sup> However, conventional garnet electrolytes suffer from reduced conductivity upon reaction with atmospheric  $\text{H}_2\text{O}/\text{O}_2$ . To address this, Han-Yi Chen et al. (2022) reported the first high-entropy garnet SSE,  $\text{Li}_{6.4}\text{La}_{3}\text{Zr}_{0.4}\text{Ta}_{0.4}\text{Nb}_{0.4}\text{Y}_{0.6}\text{W}_{0.2}\text{O}_{12}$  (LLZTNYWO). Their strategy employed multielement substitution at the Zr site using  $\text{Ta}^{5+}$ ,  $\text{Nb}^{5+}$ ,  $\text{W}^{6+}$ , and  $\text{Y}^{3+}$ , leveraging valence compensation to regulate  $\text{Li}^+$  vacancy concentration (higher valent cations increasing vacancies,  $\text{Y}^{3+}$  compensating  $\text{Li}^+$  concentration). This enhanced both stability and ionic conductivity. LLZTNYWO demonstrated a high room-temperature conductivity of  $1.16 \times 10^{-4} \text{ S cm}^{-1}$  and maintained this value after 30 days of air exposure, showcasing excellent air stability. Cyclic voltammetry (Figure 4a) revealed a wide electrochemical stability window up to 6 V versus  $\text{Li}/\text{Li}^+$ .<sup>[98]</sup> The lithium symmetric cell assembled with the LLZTNYWO electrolyte was subjected to galvanostatic cycling tests at  $0.1 \text{ mA cm}^{-2}$  and  $25^\circ\text{C}$ . The results demonstrate that the LLZTNYWO electrolyte exhibits excellent stability with low overpotential, indicating minimal interfacial resistance and good interfacial compatibility with lithium metal (Figure 4b). Furthermore, an LFP full cell assembled with the LLZTNYWO electrolyte delivered a discharge capacity of  $154 \text{ mAh g}^{-1}$  at  $0.1 \text{ C}$  ( $2\text{--}3.8 \text{ V vs Li/Li}^+$ ), reaching  $\approx 97\%$  of the capacity achieved with a conventional liquid electrolyte (Figure 4c). These findings suggest that LLZTNYWO holds significant promise for application in all-solid-state lithium batteries. Beyond single-site substitution, Chen et al. developed a related high-entropy garnet SSE, LGLTSNO, distinctively substituting Zr and Li sites in LLZO. Li/LGLTSNO/LiFePO<sub>4</sub> cells achieved 84.8% capacity retention after 100 cycles at  $0.1 \text{ C}$ , while Li symmetric cells with the LGLTSNO electrolyte exhibited stable cycling for 2000 h at  $0.1$  and  $0.1 \text{ mAh cm}^{-2}$ . LGLTSNO also exhibited superior air stability, high ionic conductivity ( $1.68 \times 10^{-4} \text{ S cm}^{-1}$  at RT), and a low interfacial resistance ( $42.3 \Omega \text{ cm}^{-2}$ ). These properties position high-entropy LGLTSNO as a promising SSE candidate for high-performance ASSBs.<sup>[99]</sup>

Although garnet electrolytes theoretically allow conductivities reaching  $10^{-3} \text{ S cm}^{-1}$ , achieving this practically is hindered by interfacial instability with electrodes, impeding  $\text{Li}^+$  transport, and elevating migration barriers. Addressing this, Liang et al. proposed a novel high-entropy fast lithium-ion conductor,  $\text{Li}_7(\text{La}, \text{Nd}, \text{Sr})_3(\text{Zr}, \text{Ta})_2\text{O}_{12}$  (LLNSZTO), exploiting high lattice distortion. Their research found that multication doping in high-entropy LLNSZTO induces lattice distortion, homogenizing lithium site energies and lowering migration barriers. This yielded an SSE with high conductivity ( $6.26 \times 10^{-4} \text{ S cm}^{-1}$ ), low activation energy (0.34 eV), and high interfacial stability. Full Li/LLNSZTO/LiFePO<sub>4</sub> cells retained 86.81% capacity after 200 cycles at room temperature (Figure 4d). ASSBs incorporating high-loading LiFePO<sub>4</sub> cathodes ( $> 12 \text{ mg cm}^{-2}$ ) achieved stable cycling for 120 cycles (Figure 4e), and pouch cells ( $5.5 \text{ cm} \times 8 \text{ cm}$ ) demonstrated stable long-term cycling with 96.5% capacity retention after 50 cycles (Figure 4f).

High-Resolution Transmission Electron Microscope (HRTEM) and strain analysis confirmed localized lattice distortion due to differently sized cations.  ${}^6\text{Li}$  NMR indicated more uniform lithium site occupancy, reflecting a flattened energy landscape for  $\text{Li}^+$  migration, thereby enhancing  $\text{Li}^+$  pathway connectivity. This study pioneered a novel “energy flattening” mechanism through high-entropy design, circumventing traditional doping limitations, and offers a new strategy for designing high-conductivity, stable SSEs to advance ASSB commercialization.<sup>[100]</sup>

### 3.3. High-Entropy Polymers

Polymer electrolytes represent a SSE system composed of a polymer matrix (e.g., PEO) and lithium salts (e.g., LiTFSI). Michael Armand first proposed the application of polymer electrolyte materials in lithium and all-solid-state batteries.<sup>[101]</sup> While offering advantages in flexibility, interfacial contact, and processability, polymer electrolytes confront challenges such as low ionic conductivity ( $\approx 10^{-7}$  to  $10^{-5} \text{ S cm}^{-1}$ ), insufficient mechanical strength, low lithium-ion mobility, significant internal concentration gradients, high interfacial impedance with electrodes, and lithium dendrite growth. Traditional improvement methods involve adding ceramic fillers (inert inorganic fillers like  $\text{Al}_2\text{O}_3$  or  $\text{SiO}_2$ ). However, Stefano Passerini noted that ceramic fillers can adversely affect interfacial stability in solvent-free systems. Active fillers (e.g., LZZO, LLTO), featuring inherent  $\text{Li}^+$  channels, effectively enhance ionic conductivity but require solutions to interfacial stability issues with lithium metal.

Yang et al. reported a novel low-enthalpy high-entropy (LEHE) electrolyte design incorporating  $\text{CsPbI}_3$  perovskite quantum dots (PQDs) into PEO-LiTFSI, forming an inorganic/organic composite electrolyte (Figure 5a). Doping with  $\text{CsPbI}_3$  significantly disrupted polymer chains, suppressed polymer crystallinity, altered polymer molecular orientation, increased structural disorder, promoted LiTFSI dissociation, weakened the strong coordination between  $\text{Li}^+$  and PEO chains, and eliminated charge concentration gradients through the low-enthalpy high-entropy design, thus imparting LEHE characteristics. This yielded a room-temperature ionic conductivity of  $1.4 \times 10^{-4} \text{ S cm}^{-1}$ —7 times higher than pure PEO—along with an increased lithium-ion transference number (from 0.19 to 0.57) and an expanded electrochemical stability window of 5.2 V (vs 4.3 V for pure PEO). Li||Li symmetric cells assembled with LEHE exhibited stable cycling for over 1000 h at  $0.3 \text{ mA cm}^{-2}$ , contrasting with pure PEO failing after 490 h. Li||LiFePO<sub>4</sub> full cells demonstrated 92.4% capacity retention after 200 cycles at  $0.5 \text{ C}$ , retained 64.2% at  $5 \text{ C}$ , and recovered 97.5% of the initial capacity upon returning to  $0.1 \text{ C}$  (Figure 5b,c). Postcycling interfacial impedance increased by only 40%, accompanied by more uniform lithium deposition. The performance is attributed to the high-entropy state reducing migration entropy, promoting segmental motion in disordered PEO chains, and forming continuous  $\text{Li}^+$  pathways. CV/GITT and AC impedance analyses confirmed reduced high-frequency polarization and facilitated rapid ion transport, with the  $\text{Li}^+$  diffusion coefficient increasing from  $1.76 \times 10^{-11}$  to  $2.75 \times 10^{-11} \text{ cm}^2 \text{ s}^{-1}$ .<sup>[102]</sup> Chen et al. (2022) employed a rock-salt phase high-entropy oxide

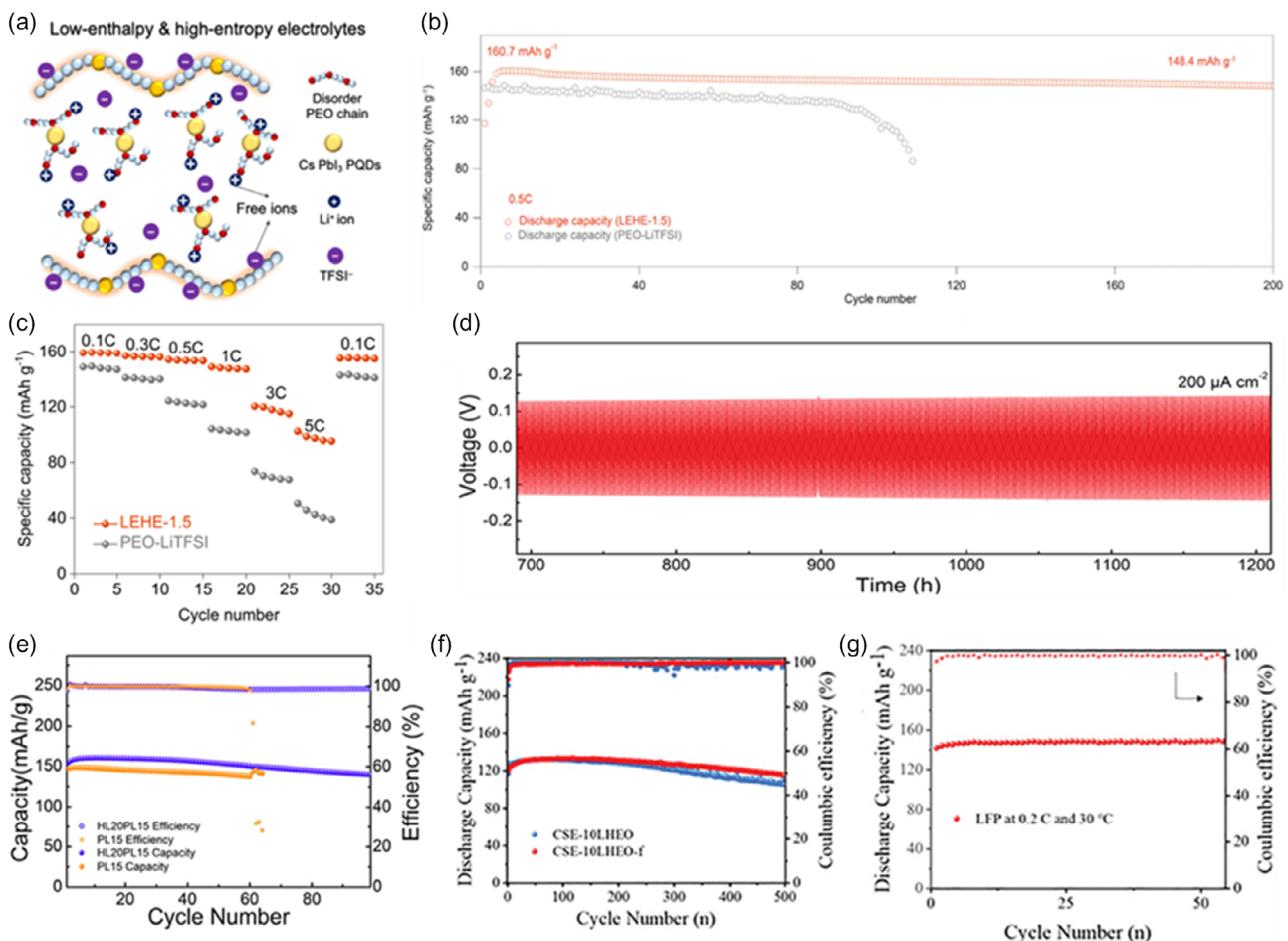


**Figure 5.** a) Structural diagram of the LEHE electrolyte. b) Cycling curve of the all-solid-state  $\text{Li}||\text{LiFePO}_4$  battery at 0.5C rate. c) Comparison of rate performance between LFP full cells assembled with LEHE electrolyte and PEO-LiTFSI. Reproduced with permission.<sup>[102]</sup> Copyright 2022, The Authors. Energy & Environmental Materials is published by John Wiley & Sons Australia, Ltd. on behalf of Zhengzhou University. d) Performance curves of a symmetric battery using HL20PL15 electrolyte at 55 °C (lithium metal surface area 1.96 cm<sup>2</sup>, constant current density 200  $\mu\text{A cm}^{-2}$ ). e) Cycling performance curve of the all-solid-state  $\text{Li}||\text{LFP}$  battery (different solid electrolytes) at 0.5C rate. Reproduced with permission.<sup>[103]</sup> Copyright 2022, American Chemical Society. f) Cycling curves of an LFP full cell using LHEO-f electrolyte at 45 °C and 2C rate. g) Cycling performance of LFP full cells based on 10-LHEO-f electrolyte at 30 °C and 0.2C rate. Reproduced with permission.<sup>[104]</sup> Copyright 2024, Wiley-VCH GmbH.

(HEO) as a filler in PEO to fabricate a solid polymer electrolyte. Incorporating this Li-containing HEO into PEO-LiTFSI yielded an electrolyte with a room-temperature ionic conductivity of  $3.44 \times 10^{-5} \text{ S cm}^{-1}$ .  $\text{Li}||\text{Li}$  symmetric cells cycled stably for 1200 h at 200  $\mu\text{A}$  with an overpotential of 140 mV, and full cells retained 91% capacity after 100 cycles at 0.5 C (Figure 5d,e).<sup>[103]</sup>

Liu et al. developed a novel microwave-assisted deep eutectic solvent (DES) method to synthesize a 2D functionalized active filler—a lamellar doped HEO rich in surface oxygen vacancies—for doping into PEO-based electrolytes. The filler's lamellar structure increased contact area with polymer chains, while oxygen vacancies enhanced interfacial interactions. Utilizing a glucose-urea DES as a 2D template enabled atomic-level mixing of multiple elements, and microwave assistance ensured uniform deposition of metal cations onto the carbon-based template. The resulting electrolyte achieved an ionic conductivity of  $2.25 \times 10^{-3} \text{ S cm}^{-1}$  at 60 °C, a  $\text{Li}^+$  transference number of 0.41, and an electrochemical window of 5.16 V. The 2D morphology enhanced interactions with PEO,

effectively suppressing crystallization and optimizing the  $\text{Li}^+$  migration environment while improving mechanical properties. Surface oxygen vacancies anchored TFSI-groups, mitigating their decomposition at interfaces and enhancing cycling stability.  $\text{Li}||\text{Li}$  symmetric cells demonstrated exceptional stability for over 2000 h.  $\text{Li}||\text{LiFePO}_4$  full cells delivered a capacity of 133.7 mAh g<sup>-1</sup> at 2C (45 °C) with 87.34% retention after 500 cycles. At near room temperature (30 °C, 0.2 C), the cell delivered a peak capacity of 149.4 mAh g<sup>-1</sup> with an average Coulombic efficiency exceeding 99.5% and no capacity decay over 50 cycles, showcasing outstanding rate capability and cycling performance (Figure 5f,g).<sup>[104]</sup>

#### 4. Introduction High-Entropy Material Enabled Protection Strategies for Li Anodes

Lithium metal is recognized as an ideal anode material for high-energy-density batteries, owing to its exceptionally high theoretical specific capacity (3860 mAh g<sup>-1</sup>) and low thermodynamic

equilibrium potential ( $-3.04\text{ V}$  vs the standard hydrogen electrode).<sup>[105]</sup> Nevertheless, it suffers from high chemical reactivity that triggers continuous parasitic reactions with organic electrolytes.<sup>[106]</sup> This leads to irreversible loss of active lithium and heterogeneous growth of the SEI. The resulting SEI typically exhibits a loosely packed structure with inadequate mechanical stability, rendering it prone to fracture during repeated volume changes associated with lithium deposition/stripping cycles. Fresh lithium surfaces exposed at fracture sites further accelerate parasitic reactions.<sup>[107]</sup> This vicious cycle induces heterogeneous spatial distribution of lithium-ion flux, triggering vertically oriented growth of lithium dendrites, ultimately culminating in battery capacity fading and safety hazards.<sup>[108]</sup> Existing solutions primarily include interfacial modification (constructing artificial protective layers) and lithium metal substitution (developing alloy/composite anodes). However, both face fundamental challenges—single-component materials struggle to simultaneously meet multidimensional performance requirements (e.g., ionic conduction, mechanical strength, interfacial stability).<sup>[109,110]</sup> Recent innovations in material design paradigms offer a promising approach to overcome this impasse: introducing multicomponent synergistic strategies enables the atomic-scale construction of functional systems with adaptive properties. Multicomponent systems dynamically regulate SEI composition distribution in interfacial engineering through competitive reactions, forming gradient protection layers. For lithium substitution, the phase-transition synergy in high-entropy materials effectively suppresses volumetric expansion.

#### 4.1. Protective Layers

Anode interface engineering focuses on designing artificial functional layers to regulate uniform lithium deposition behavior. Current research has significantly enhanced the cycling stability of lithium metal anodes through interfacial layers incorporating metallic alloys (e.g., Li–Mg/Li–Zn), inorganic compounds (Li<sub>3</sub>N/LiF), and organic–inorganic composites.<sup>[111]</sup> An ideal interface must fulfill multifunctional requirements: 1) homogeneously distributed active sites guiding uniform lithium nucleation; 2) structural properties balancing rigidity and toughness to suppress dendrite penetration; and 3) chemically inert surfaces blocking electrolyte decomposition side reactions. However, single-component materials struggle to optimize these properties simultaneously, necessitating synergistic multicomponent strategies for integrated functional design.

HEAs exhibit unique advantages through multicomponent synergy. Lithiophilic elements (e.g., Al, Zn) promote uniform nucleation via strong adsorption, while magnetic elements (Co, Ni, Fe) construct field-responsive interfaces that regulate lithium-ion transport pathways through Lorentz forces, inhibiting dendrite growth. High configurational entropy further endows HEAs with exceptional mechanical strength and corrosion resistance. Conventional HEA synthesis (e.g., high-temperature processing, high-energy ball milling) faces compatibility issues with lithium substrates due to temperatures exceeding lithium's melting point or nonuniform coatings from mechanical alloying.<sup>[112]</sup>

Addressing this challenge, Chen and colleagues developed an Al–Zn–Co–Ni–Fe multicomponent interfacial layer on lithium metal via room-temperature magnetron sputtering. Combining DFT and experimental characterization, the design principles were systematically elucidated: Adsorption energy analysis revealed stronger lithium affinity for Al and Zn (Figure 6a), providing thermodynamic driving forces for preferential adsorption and uniform deposition. Vibrating sample magnetometry confirmed the ferromagnetic behavior of AZCNF, with its narrow hysteresis loop and saturation magnetization of  $21.52\text{ emu g}^{-1}$  (Figure 6b), demonstrating magnetic-element-induced Lorentz force modulation of Li<sup>+</sup> transport. This multielement cocktail effect engineered the AZCNF interfacial phase,<sup>[113]</sup> which integrates triple functions: 1) lithiophilic sites optimizing Li<sup>+</sup> flux distribution; 2) magnetic elements inducing horizontal Lorentz forces to suppress vertical dendrite growth; and 3) high mechanical strength and corrosion resistance ensuring interfacial stability. AZCNF-modified anodes achieved stable cycling for over 4000 h at  $2\text{ mA cm}^{-2}$  (Figure 6c). When paired with LiFePO<sub>4</sub> cathodes, full cells retained  $\approx 90\%$  capacity after 300 cycles at 1 C with a coulombic efficiency of 99.7% and delivered excellent rate capability across 0.1 C–4 C (Figure 6d,e).

Further optimizing this approach, Zheng et al. employed particle swarm optimization to determine optimal sputtering parameters (power, duration, substrate rotation) and composition ratio (Al:Zn:Fe:Co:Ni = 7:5:4:3:1) for dense HEA layers.<sup>[114]</sup> The optimized HEA@Li symmetric cell cycled stably for 2400 h at  $1\text{ mA cm}^{-2}/1\text{ mAh cm}^{-2}$ , while Li||LFP full cells retained  $>90\%$  capacity after 300 cycles. Similarly, Wang et al. engineered a dynamic adsorption network via gradient adsorption energy distribution ( $-3.18$  to  $-2.03\text{ eV}$ ), developing ultrasmooth 20 nm HEA nanoparticles (NiCdCuInZn) on carbon fiber (HEA/C) through thermodynamic phase transition. Gradient active sites enabled selective binding with low nucleation barriers, while multiple transport pathways facilitated uniform lithium deposition. Consequently, HEA/C demonstrated high reversibility over 2000 cycles, achieving 99.6% Coulombic efficiency in asymmetric cells ( $5\text{ mA cm}^{-2}/1\text{ mAh cm}^{-2}$ ) and exceeding 7200 h in symmetric cells ( $60\text{ mA cm}^{-2}/60\text{ mAh cm}^{-2}$ ).<sup>[115]</sup>

For mechanical stability enhancement, the high configurational entropy characteristic of HEAs improves deformation resistance at interfaces through synergistic elemental interactions. Cheng et al. developed an HEMP (NiCoFeSnSbP)@RGO-MTL@PH substrate,<sup>[116]</sup> employing interfacial coupling between reduced graphene oxide (RGO) and a multicomponent HEA coating to achieve uniform stress distribution. In situ optical microscopy observations confirmed the absence of lithium dendrite growth during cycling. Cross-sectional scanning electron microscopy analysis further demonstrated that the interfacial layer remained free of cracks or delamination, while the deposited lithium maintained a dense and uniform morphology, effectively suppressing mechanical failure induced by volumetric expansion.

Beyond lithium metal interface engineering, HEA designs also demonstrate unique regulatory advantages for sodium metal anodes. Ge et al.<sup>[117]</sup> leveraged crystal facet boundary

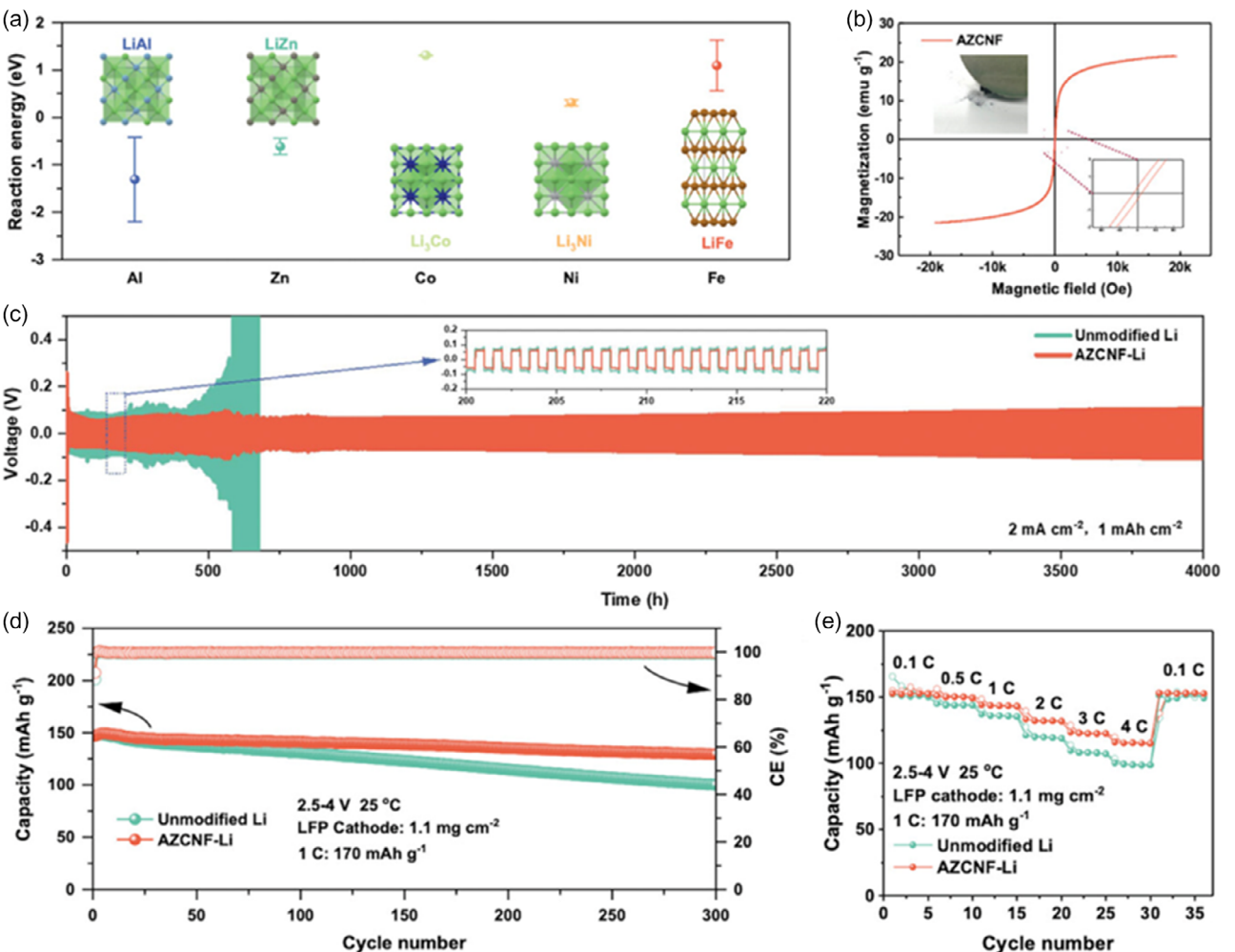


**Figure 6.** a) Computed reaction energies for lithium alloy formation with selected elements. b) Magnetization hysteresis profile of AZCNF material. c) Long-term cycling behavior of symmetric cells at  $2 \text{ mA cm}^{-2}$ . d) Cyclic stability comparison of  $\text{Li}||\text{LFP}$  full cells featuring unmodified versus AZCNF-modified Li anodes. e) Rate capability assessment of the cells. Reproduced with permission.<sup>[113]</sup> Copyright 2024, Wiley-VCH GmbH.

engineering between (100)/(101) planes at zinc-flower edge structures to induce the formation of a highly dense, reversible inorganic interfacial layer (comprising  $\text{ZnF}_2$ ,  $\text{NaZn}_{13}$ ,  $\text{NaF}$ ,  $\text{Na}_2\text{CO}_3$ ) for sodium deposition. Similarly, Liu et al. constructed a 708 nm thick interfacial layer of NbMoTaWV pentanary HEA on an aluminum current collector via magnetron sputtering, effectively addressing sodium dendrite growth and SEI dynamic stability issues. This approach provides a new paradigm for designing high-energy-density sodium metal and sodium-air batteries.

#### 4.2. Alternative Lithium-Based Anodes

Dendrite growth in lithium metal anodes severely compromises cycling stability and safety in lithium–oxygen and lithium-ion batteries.<sup>[118]</sup> Drawing inspiration from intercalation anode design principles in lithium-ion batteries, replacing lithium metal with high-entropy materials effectively circumvents dendrite risks. High-entropy materials leverage

synergistic lattice effects of multiple metallic components to construct stable framework structures with dynamic stress-buffering capabilities. The cooperative action of multiactive sites optimizes uniform lithium-ion deposition pathways. It achieves intelligent volume strain regulation through multi-scale structural design, providing innovative solutions for high-safety anode systems.

In 2015, Rost et al. pioneered the synthesis of a high-entropy rock-salt oxide ( $\text{Co}_{0.2}\text{Cu}_{0.2}\text{Mg}_{0.2}\text{Ni}_{0.2}\text{Zn}_{0.2}\text{O}$ )<sup>[45]</sup> confirming the random homogeneous distribution of five metal cations within the lattice and demonstrating entropy-driven effects governing reversible phase transitions in this single-phase solid solution. Sarkar et al. first employed this HEO as an anode material in lithium-ion batteries.<sup>[119]</sup> In situ X-ray diffraction (XRD) and selected-area electron diffraction (SAED) analyses verified the exceptional structural stability of the rock-salt framework during lithiation/delithiation (Figure 7a), enabling stable cycling over 500 cycles at  $0.2 \text{ A g}^{-1}$  (Figure 7b). In contrast, the quaternary system

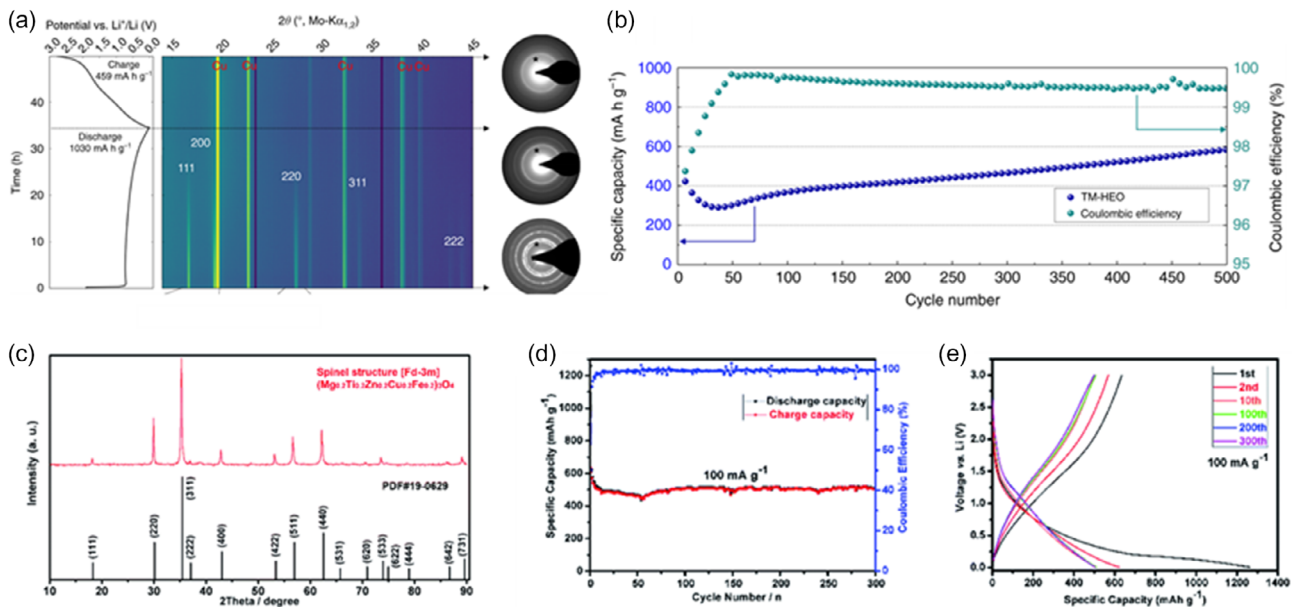


**Figure 7.** a) In situ XRD during the first lithiation/delithiation cycle. Arrows mark as-prepared, fully lithiated, and delithiated states on the time-dependent potential profile (left). XRD reflections progressively diminish during initial lithiation and disappear after the first cycle. Corresponding SAED patterns (right) show significantly smaller crystallites detectable due to electrons' shorter wavelength. The asterisk denotes a persistent (200) rock-salt lattice plane throughout the process. b) Cycling stability and Coulombic efficiency of calcined TM-HEO at 200 mA g<sup>-1</sup>. Reproduced with permission.<sup>[119]</sup> Copyright 2018, The Author(s). c) XRD diffraction pattern of (Mg<sub>0.2</sub>Ti<sub>0.2</sub>Zn<sub>0.2</sub>Cu<sub>0.2</sub>Fe<sub>0.2</sub>)<sub>3</sub>O<sub>4</sub> particles. d) Cycling stability and corresponding coulombic efficiency over 300 cycles at 100 mA g<sup>-1</sup>. e) Discharge-charge voltage profiles recorded at the 1st, 2nd, 10th, 100th, 200th, and 300th cycles within a voltage window of 0.01–3.00 V and a current density of 100 mA g<sup>-1</sup>. Reproduced with permission.<sup>[121]</sup> Copyright 2020, RSC Adv.

(Cu<sub>0.25</sub>Mg<sub>0.25</sub>Ni<sub>0.25</sub>Zn<sub>0.25</sub>)O exhibited significant capacity decay due to the absence of high-entropy stabilization, validating multicomponent synergy in reinforcing structural integrity. Spinel-structure HEOs, featuring two distinct cation Wyckoff sites, exhibit kinetically optimized 3D Li<sup>+</sup> diffusion channels facilitated by synergistic interactions of multivalent metals.<sup>[120]</sup> Chen et al. reported the first spinel HEO anode (Mg<sub>0.2</sub>Ti<sub>0.2</sub>Zn<sub>0.2</sub>Cu<sub>0.2</sub>Fe<sub>0.2</sub>)<sub>3</sub>O<sub>4</sub> (XRD Figure 7c) with aliovalent cations,<sup>[121]</sup> delivering a substantial reversible capacity of 504 mAh g<sup>-1</sup> through mixed Fe<sup>3+</sup>/Ti<sup>4+</sup> valence states and poly-metallic synergy. However, the presence of inactive Mg limited overall energy density (Figure 7d,e). Electrochemical performance can be tailored by strategic element selection: active components (e.g., Fe, Cu) primarily contribute capacity via redox reactions and alloying, while inactive elements (e.g., Mg, Al) stabilize the crystalline framework and inhibit particle aggregation.<sup>[122]</sup>

Perovskite-type HEOs offer greater design flexibility than spinel compositional constraints due to their unique structural tunability. Yan et al. synthesized [(Bi, Na)<sub>1/5</sub>(La, Li)<sub>1/5</sub>(Ce, K)<sub>1/5</sub>Ca<sub>1/5</sub>Sr<sub>1/5</sub>]TiO<sub>3</sub>,<sup>[123]</sup> demonstrating superior electrochemical performance in lithium-ion batteries. Jia et al. advanced this approach with RE(Co<sub>0.2</sub>Cr<sub>0.2</sub>Fe<sub>0.2</sub>Mn<sub>0.2</sub>Ni<sub>0.2</sub>)O<sub>3</sub> (RE = La, Sm, Gd). This system features a mesoporous structure with significant lattice distortion and controllable oxygen vacancies, providing abundant ion transport pathways and delivering 403 mAh g<sup>-1</sup> after 500 cycles at 0.2 A g<sup>-1</sup>. Regulating the balance between lattice distortion and oxygen vacancies further modulates lithium-ion storage performance, offering a promising pathway for breakthroughs in high-entropy anode materials.

## 5. Summary and Outlook

In this review, we first elucidate the fundamental reaction mechanisms of lithium-oxygen (Li-O<sub>2</sub>) batteries and the core challenges facing their cathode catalysts, electrolytes, and anodes. HEAs demonstrate multifunctional advantages across these components: serving as catalysts to significantly accelerate ORR/OER reaction kinetics; enhancing ionic conductivity in electrolytes; and suppressing lithium dendrite growth at the anode through dual strategies—constructing artificial protective layers and replacing lithium metal. Despite significant progress of HEAs in Li-O<sub>2</sub> batteries, critical issues regarding their reaction mechanisms and long-term stability require further investigation. The review concludes with future perspectives on HEAs to overcome current scientific bottlenecks: 1) The vast compositional design space of HEA catalysts renders traditional trial-and-error approaches inherently vulnerable to stochastic variability and systematic bias. Machine learning and theoretical computations provide efficient solutions: machine learning facilitates rapid screening of catalytic activities across diverse elemental combinations by constructing performance prediction models, guiding experimental design and material synthesis, while optimizing compositions and processing parameters to enhance performance and research efficiency. Complementarily, theoretical computations leverage high-throughput quantum mechanics and molecular dynamics simulations to probe, at the atomic scale, the microstructural evolution, phase transitions, and changes in adsorption energies (i.e., reaction activation energies) of reaction intermediates at

HEAs active sites. Integrating these methods enables rational design of element types and ratios, effectively tuning catalytic performance, mechanical properties, corrosion resistance, and thermal stability, thereby achieving intelligent design and performance leapfrogging of HEAs for Li–O<sub>2</sub> batteries. 2) The catalytic activity of HEAs in Li–O<sub>2</sub> batteries primarily depends on surface adsorption and electron transfer processes, yet the underlying mechanisms remain unclear. A key challenge lies in regulating *d*-band center shifts and optimizing reactant/intermediate adsorption energies to enhance ORR/OER. Elucidating electronic structure control principles is imperative, and *in situ* surface characterization techniques offer crucial means to address this. Real-time tracking of dynamic catalyst evolution reveals the role of metal atoms and guides activity modulation. For example, *in situ* XRD monitors the formation and decomposition of products during reactions; *in situ* electron microscopy captures the growth trajectories and compositional evolution of intermediates/final products on catalyst surfaces; XPS and absorption spectroscopy resolve valence state fluctuations and electronic structure reconstruction during cycling. Concurrently, deciphering the micromechanisms of dynamic interface evolution necessitates developing spatiotemporal multiscale *in situ* characterization techniques (e.g., operando synchrotron-based X-ray absorption spectroscopy, cryogenic electron microscopy) to track, in real time, the chemical state evolution at electrode/electrolyte interfaces, lattice distortion relaxation behavior, and dendrite suppression dynamics during cycling, thereby establishing quantitative correlation models between failure mechanisms and material properties. 3) The breakthrough characteristics of HEAs should be extended beyond lithium-based systems to metal–air batteries, including sodium, magnesium, and iron-based chemistries, opening new opportunities. HEAs could simultaneously address sodium dendrite suppression and oxygen reaction kinetics through multicomponent synergy in sodium–oxygen and sodium–carbon dioxide batteries. Specifically designed HEA catalysts may modulate the adsorption behavior of oxygen intermediates, while disordered channels in high-entropy solid electrolytes might enhance low-temperature sodium ion transport. For magnesium–oxygen batteries, the dynamic interfacial properties of high-entropy materials offer solutions to persistent passivation layer issues. Engineered element combinations could enable self-adaptive protective layers that remove deposition products on magnesium anodes. Regarding iron–oxygen batteries, HEA entropic stabilization effects may suppress side reactions at iron electrodes and stabilize iron ion redox processes via multielement synergistic carriers. This cross-system applicability stems from fundamental HEA traits—composition tunability enables tailoring chemical microenvironments to specific metal ions. At the same time, lattice distortion universally optimizes multivalent ion migration, and entropic stabilization maintains structural integrity under thermal extremes. Future research should prioritize developing theoretical frameworks that apply established lithium–oxygen battery principles, such as lattice modulation strategies and interfacial evolution dynamics, to emerging sodium–air, magnesium–air, and iron–air battery systems.

## Acknowledgements

The authors gratefully acknowledge Sponsored by Shanghai Rising-Star Program. This research was financially supported by the National Natural Science Foundation of China (52173173 and 22309110), the Natural Science Foundation of Jiangsu Province (BK20220051), the Postdoctoral Fellowship Program of CPSF under grant number GZC20241001, and the China Postdoctoral Science Foundation (2024M761974).

## Conflict of Interest

The authors declare no conflict of interest.

**Keywords:** anode protection • catalysis • electrolytes • high-entropy alloys • lithium–oxygen batteries

- [1] K. M. Abraham, Z. Jiang, *J. Electrochem. Soc.* **1996**, *143*, 1.
- [2] M. Armand, J. M. Tarascon, *Nature* **2008**, *451*, 652.
- [3] K. Song, D. A. Agyeman, M. Park, J. Yang, Y. Kang, *Adv. Mater.* **2017**, *29*, 1606572.
- [4] L. G. Cota, P. De La Mora, *Acta Crystallogr. B* **2005**, *61*, 133.
- [5] X. Ren, S. S. Zhang, D. T. Tran, J. Read, *J. Mater. Chem.* **2011**, *21*, 10118.
- [6] Z. Lyu, Y. Zhou, W. Dai, X. Cui, M. Lai, L. Wang, F. Huo, W. Huang, Z. Hu, W. Chen, *Chem. Soc. Rev.* **2017**, *46*, 6046.
- [7] K. Amine, R. Kanro, Y. Tzeng, *MRS Bull.* **2014**, *39*, 395.
- [8] C. Ó. Laoire, S. Mukerjee, E. J. Plichta, M. A. Hendrickson, K. M. Abraham, *J. Electrochem. Soc.* **2011**, *158*, A302.
- [9] P. Ju, Y. Su, C. Qin, *J. Hohai Univ.* **2018**, *3*, 12.
- [10] X. Gao, Y. Chen, L. R. Johnson, Z. P. Jovanov, P. G. Bruce, *Nat. Energy* **2017**, *2*, 17118.
- [11] J. Lu, L. Li, J. B. Park, Y. K. Sun, F. Wu, K. Amine, *Chem. Rev.* **2014**, *114*, 5611.
- [12] Z. Zhang, X. Xiao, A. Yan, K. Sun, J. Yu, P. Tan, *Nat. Commun.* **2024**, *15*, 9952.
- [13] J. Chen, C. Chen, T. Huang, A. Yu, *ACS Omega* **2019**, *4*, 20708.
- [14] V. Viswanathan, J. K. Nørskov, A. Speidel, R. Scheffler, S. Gowda, A. C. Luntz, *J. Phys. Chem. Lett.* **2013**, *4*, 556.
- [15] L. Grande, E. Paillard, J. Hassoun, J. Park, Y. Lee, Y. Sun, S. Passerini, B. Scrosati, *Adv. Mater.* **2015**, *27*, 784.
- [16] P. G. Bruce, S. A. Freunberger, L. J. Hardwick, J. M. Tarascon, *Nat. Mater.* **2012**, *11*, 19.
- [17] Y. Ko, K. Kim, J. Yoo, G. Kwon, H. Park, J. Kim, B. Lee, J. H. Song, J. Kim, K. Kang, *Energy Environ. Sci.* **2023**, *16*, 5525.
- [18] C. Xia, R. Black, R. Fernandes, B. Adams, L. F. Nazar, *Nat. Chem.* **2015**, *7*, 496.
- [19] L. Johnson, C. Li, Z. Liu, Y. Chen, S. A. Freunberger, P. C. Ashok, B. B. Praveen, K. Dholakia, J. M. Tarascon, P. G. Bruce, *Nat. Chem.* **2014**, *6*, 1091.
- [20] B. D. McCloskey, A. Valery, A. C. Luntz, S. R. Gowda, G. M. Wallraff, J. M. Garcia, T. Mori, L. E. Krupp, *J. Phys. Chem. Lett.* **2013**, *4*, 2989.
- [21] P. G. Bruce, *Solid State Ion.* **2008**, *179*, 752.
- [22] J. M. Tarascon, M. Armand, *Nature* **2001**, *414*, 359.
- [23] M. S. Whittingham, *Chem. Rev.* **2004**, *104*, 4271.
- [24] F. Wu, J. T. Lee, N. Nitta, H. Kim, O. Borodin, G. Yushin, *Adv. Mater.* **2015**, *27*, 101.
- [25] L. Li, C. Chen, A. Yu, *Sci. China Chem.* **2017**, *60*, 1402.
- [26] A. C. Luntz, B. D. McCloskey, *Chem. Rev.* **2014**, *114*, 11721.
- [27] H. Dai, X. Gu, J. Dong, C. Wang, C. Lai, S. Sun, *Nat. Commun.* **2020**, *11*, 643.
- [28] W. J. Kwak, H. J. Shin, J. Reiter, N. Tsiovaras, J. Hassoun, S. Passerini, B. Scrosati, Y. K. Sun, *J. Mater. Chem. A* **2016**, *4*, 10467.
- [29] H. Zhang, G. G. Eshetu, X. Judez, C. Li, L. M. Rodriguez-Martínez, M. Armand, *Angew. Chem. Int. Ed.* **2018**, *57*, 15002.
- [30] J. Ma, C. Huang, *J. Energy Storage* **2023**, *66*, 107419.
- [31] M. Fu, X. Ma, K. Zhao, X. Li, D. Su, *iScience* **2021**, *24*, 102177.
- [32] Y. Yao, J. Chen, R. Niu, Z. Zhao, X. Wang, *Metals* **2023**, *13*, 833.

- [33] A. Kausar, M. H. Eisa, O. Aldaghri, K. H. Ibnaouf, A. Mimouni, *Results Phys.* **2024**, *62*, 107838.
- [34] J. W. Yeh, *JOM* **2013**, *65*, 1759.
- [35] W. T. Zhang, X. Q. Wang, F. Q. Zhang, X. Y. Cui, B. B. Fan, J. M. Guo, Z. M. Guo, R. Huang, W. Huang, X. B. Li, M. R. Li, Y. Ma, Z. H. Shen, Y. G. Sun, D. Z. Wang, F. Y. Wang, L. Q. Wang, N. Wang, T. L. Wang, W. Wang, X. Y. Wang, Y. H. Wang, F. J. Yu, Y. Z. Yin, L. K. Zhang, Y. Zhang, J. Y. Zhang, Q. Zhao, Y. P. Zhao, X. D. Zhu, et al., *Rare Met.* **2024**, *43*, 4639.
- [36] E. P. George, D. Raabe, R. O. Ritchie, *Nat. Rev. Mater.* **2019**, *4*, 515.
- [37] Y. Li, Z. Luo, S. E. Skrabalak, Y. Xiong, *ACS Mater. Lett.* **2024**, *6*, 2696.
- [38] J.-W. Yeh, S.-K. Chen, S.-J. Lin, J.-Y. Gan, T.-S. Chin, T.-T. Shun, C.-H. Tsau, S.-Y. Chang, *Adv. Eng. Mater.* **2004**, *6*, 299.
- [39] B. Ouyang, Y. Zeng, *Nat. Commun.* **2024**, *15*, 973.
- [40] A. Marshal, K. G. Pradeep, D. Music, S. Zaeferer, P. S. De, J. M. Schneider, *J. Alloys Compd.* **2017**, *691*, 683.
- [41] L. Jiang, Y. P. Lu, H. Jiang, T. M. Wang, B. N. Wei, Z. Q. Cao, T. J. Li, *Mater. Sci. Technol.* **2016**, *32*, 588.
- [42] C. Y. Cheng, Y. C. Yang, Y. Z. Zhong, Y. Y. Chen, T. Hsu, J. W. Yeh, *Curr. Opin. Solid State Mater. Sci.* **2017**, *21*, 299.
- [43] K. X. Yin, Z. W. Huang, B. L. Wu, G. J. Zhang, Q. W. Tian, Y. N. Wang, *Acta Mater.* **2024**, *263*, 119445.
- [44] K. X. Yin, G. Y. Dong, G. J. Zhang, Q. W. Tian, Y. N. Wang, J. C. Huang, *J. Mater. Res. Technol.* **2023**, *24*, 7654.
- [45] C. M. Rost, E. Sachet, T. Borman, A. Moballegh, E. C. Dickey, D. Hou, J. L. Jones, S. Curtarolo, J. P. Maria, *Nat. Commun.* **2015**, *6*, 8485.
- [46] B. Feng, M. Widom, *Mater. Chem. Phys.* **2018**, *210*, 309.
- [47] P. Li, J. Hu, G. Huang, J. Zhang, W. Wang, C. Tian, H. Xiao, X. Zhou, H. Shen, X. Long, S. Peng, X. Zu, *J. Alloys Compd.* **2022**, *905*, 164150.
- [48] C. C. Yen, G. R. Huang, Y. C. Tan, H. W. Yeh, D. J. Luo, K. T. Hsieh, E. W. Huang, J. W. Yeh, S. J. Lin, C. C. Wang, C. L. Kuo, S. Y. Chang, Y. C. Lo, *J. Alloys Compd.* **2020**, *818*, 152876.
- [49] C. Lee, G. Song, M. C. Gao, R. Feng, P. Chen, J. Brecht, Y. Chen, K. An, W. Guo, J. D. Poplawsky, S. Li, A. T. Samaei, W. Chen, A. Hu, H. Choo, P. K. Liaw, *Acta Mater.* **2018**, *160*, 158.
- [50] H. Oh, D. Ma, G. Leyson, B. Grabowski, E. Park, F. Körmann, D. Raabe, *Entropy* **2016**, *18*, 321.
- [51] H. Wang, Q. He, X. Gao, Y. Shang, W. Zhu, W. Zhao, Z. Chen, H. Gong, Y. Yang, *Adv. Mater.* **2024**, *36*, 2305453.
- [52] J. Dąbrowa, M. Zajusz, W. Kucza, G. Cieślak, K. Berent, T. Czeppe, T. Kulik, M. Danielewski, *J. Alloys Compd.* **2019**, *783*, 193.
- [53] A. Mehta, Y. Sohn, *ACS Comb. Sci.* **2020**, *22*, 757.
- [54] Q. Li, W. Chen, J. Zhong, L. Zhang, Q. Chen, Z. K. Liu, *Metals* **2017**, *8*, 16.
- [55] C. G. Schön, M. A. Tunes, R. Arróyave, J. Ågren, *Calphad* **2020**, *68*, 101713.
- [56] D. L. Beke, G. Erdélyi, *Mater. Lett.* **2016**, *164*, 111.
- [57] J. Dąbrowa, M. Danielewski, *Metals* **2020**, *10*, 347.
- [58] W. Kucza, J. Dąbrowa, G. Cieślak, K. Berent, T. Kulik, M. Danielewski, *J. Alloys Compd.* **2018**, *731*, 920.
- [59] L. Wang, L. Zhang, X. Lu, F. Wu, X. Sun, H. Zhao, Q. Li, *Chem. Eng. J.* **2023**, *465*, 142766.
- [60] C. B. Chang, Y. R. Lu, H. Y. Tuan, *Energy Storage Mater.* **2023**, *59*, 102770.
- [61] W. L. Hsu, C. W. Tsai, A. C. Yeh, J. W. Yeh, *Nat. Rev. Chem.* **2024**, *8*, 471.
- [62] Y. Wang, L. Zang, S. Dou, L. Hao, *Appl. Energy* **2025**, *391*, 125934.
- [63] Y. Wang, Y. Lu, *Angew. Chem. Int. Ed.* **2019**, *58*, 6962.
- [64] B. M. Gallant, D. G. Kwabi, R. R. Mitchell, J. Zhou, C. V. Thompson, Y. Shao-Horn, *Energy Environ. Sci.* **2013**, *6*, 2518.
- [65] R. Cao, L. Liu, W. Yu, S. Ding, *SusMat* **2025**, *5*, e251.
- [66] J. Chen, E. Quattrochi, F. Ciucci, Y. Chen, *Chem* **2023**, *9*, 2267.
- [67] A. Dutta, K. Ito, A. Nomura, Y. Kubo, *Adv. Sci.* **2020**, *7*, 2001660.
- [68] D. Wang, X. Mu, P. He, H. Zhou, *Mater. Today* **2019**, *26*, 87.
- [69] Y. Zhou, S. Guo, *eScience* **2023**, *3*, 100123.
- [70] M. Chen, N. Kitiphatpiboon, C. Feng, A. Abudula, Y. Ma, G. Guan, *eScience* **2023**, *3*, 100111.
- [71] L. Liu, C. Zhou, W. Fang, Y. Hou, Y. Wu, *Energy Mater.* **2023**, *3*, 300011.
- [72] P. Liu, C. Wang, C. Zeng, S. Wang, X. Yu, H. Xiao, Y. Huang, Y. Zhang, Y. Zeng, C. Shu, Z. Liang, *SusMat* **2025**, *5*, e70007.
- [73] C. Dang, Q. Mu, X. Xie, X. Sun, X. Yang, Y. Zhang, S. Maganti, M. Huang, Q. Jiang, I. Seok, W. Du, C. Hou, *Adv. Compos. Hybrid Mater.* **2022**, *5*, 606.
- [74] Y. C. Lu, Z. Xu, H. A. Gasteiger, S. Chen, K. Hamad-Schifferli, Y. Shao-Horn, *J. Am. Chem. Soc.* **2010**, *132*, 12170.
- [75] Y. C. Lu, H. A. Gasteiger, Y. Shao-Horn, *J. Am. Chem. Soc.* **2011**, *133*, 19048.
- [76] B. Sun, P. Munroe, G. Wang, *Sci. Rep.* **2013**, *3*, 2247.
- [77] D. Oh, K. Virwani, L. Tadesse, M. Jurich, N. Aetukuri, L. E. Thompson, H. C. Kim, D. S. Bethune, *J. Phys. Chem. C* **2017**, *121*, 1404.
- [78] S. Ma, Y. Wu, J. Wang, Y. Zhang, Y. Zhang, X. Yan, Y. Wei, P. Liu, J. Wang, K. Jiang, S. Fan, Y. Xu, Z. Peng, *Nano Lett.* **2015**, *15*, 8084.
- [79] J. Tian, Y. Rao, W. Shi, J. Yang, W. Ning, H. Li, Y. Yao, H. Zhou, S. Guo, *Angew. Chem. Int. Ed.* **2023**, *62*, e202310894.
- [80] D. Du, H. He, R. Zheng, L. Zeng, X. Wang, C. Shu, C. Zhang, *Adv. Energy Mater.* **2024**, *14*, 2304238.
- [81] H. Xu, X. Wang, G. Tian, F. Fan, X. Wen, P. Liu, C. Shu, *ACS Nano* **2024**, *18*, 27804.
- [82] G. Feng, F. Ning, J. Song, H. Shang, K. Zhang, Z. Ding, P. Gao, W. Chu, D. Xia, *J. Am. Chem. Soc.* **2021**, *143*, 17117.
- [83] H. Ge, W. Shi, J. Liu, Y. Zhang, X. Wang, *J. Am. Chem. Soc.* **2025**, *147*, 8367.
- [84] L. Tao, M. Sun, Y. Zhou, M. Luo, F. Lv, M. Li, Q. Zhang, L. Gu, B. Huang, S. Guo, *J. Am. Chem. Soc.* **2022**, *144*, 10582.
- [85] X. Yan, Y. Zhou, S. Wang, *Adv. Funct. Mater.* **2025**, *35*, 2413115.
- [86] H. Li, H. Huang, Y. Chen, F. Lai, H. Fu, L. Zhang, N. Zhang, S. Bai, T. Liu, *Adv. Mater.* **2023**, *35*, 2209242.
- [87] M. Marcinek, J. Syzdek, M. Marczewski, M. Piszcza, L. Niedzicki, M. Kalita, A. Plewa-Marczewska, A. Bitner, P. Wieczorek, T. Trzeciak, M. Kasprzyk, *Solid State Ion.* **2015**, *276*, 107.
- [88] M. Alvarez-Tirado, L. Castro, G. Guzman-Gonzalez, A. Gueguen, L. C. Tome, D. Mecerreyres, *Energy Mater.* **2022**, *3*, 300003.
- [89] Q. Zhang, Y. Huang, H. Hu, C. Ma, Y. Zhong, P. Wu, W. Lv, F. Li, X. Liu, *eScience* **2025**, 100457.
- [90] G. Leverick, Y. Shao-Horn, *Adv. Energy Mater.* **2023**, *13*, 2204094.
- [91] J. Zhou, H. Wang, Y. Yang, X. Li, C. Guo, Z. Li, S. Wen, J. Cai, Z. Wang, Y. Zhang, Q. Huang, Z. Zheng, *Adv. Energy Mater.* **2025**, *11*, 2410129.
- [92] P. Phogat, S. Rawat, B. Chand, *J. Energy Storage* **2025**, *130*, 117314.
- [93] Q. Wang, C. Zhao, Z. Yao, J. Wang, F. Wu, S. G. H. Kumar, S. Ganapathy, S. Eustace, X. Bai, B. Li, J. Lu, M. Wagemaker, *Adv. Mater.* **2023**, *35*, 2210677.
- [94] Q. Wang, C. Zhao, J. Wang, Z. Yao, S. Wang, S. G. H. Kumar, S. Ganapathy, S. Eustace, X. Bai, B. Li, M. Wagemaker, *Nat. Commun.* **2023**, *14*, 440.
- [95] S. C. Kim, J. Wang, R. Xu, P. Zhang, Y. Chen, Z. Huang, Y. Yang, Z. Yu, S. T. Oyakhire, W. Zhang, L. C. Greenburg, M. S. Kim, D. T. Boyle, P. Sayavong, Y. Ye, J. Qin, Z. Bao, Y. Cui, *Nat. Energy* **2023**, *8*, 814.
- [96] V. Thangadurai, H. Kaack, W. J. F. Weppner, *J. Am. Ceram. Soc.* **2003**, *86*, 437.
- [97] R. Murugan, V. Thangadurai, W. Weppner, *Angew. Chem. Int. Ed.* **2007**, *46*, 7778.
- [98] C. H. Kuo, A. Y. Wang, H. Y. Liu, S. C. Huang, X. R. Chen, C. C. Chi, Y. C. Chang, M. Y. Lu, H. Y. Chen, *APL Mater.* **2022**, *10*, 121104.
- [99] S. Yu, Y. Li, J. Luo, D. Chen, L. Yang, Y. Wei, D. Li, Y. Li, Y. Chen, *J. Energy Chem.* **2024**, *96*, 414.
- [100] S. Wang, X. Wen, Z. Huang, H. Xu, F. Fan, X. Wang, G. Tian, S. Liu, P. Liu, C. Wang, C. Zeng, C. Shu, Z. Liang, *Adv. Funct. Mater.* **2025**, *35*, 2416389.
- [101] A. Mauger, C. M. Julien, J. B. Goodenough, K. Zaghib, *J. Electrochem. Soc.* **2020**, *167*, 070507.
- [102] H. Zhang, Y. Wang, J. Huang, W. Li, X. Zeng, A. Jia, H. Peng, X. Zhang, W. Yang, *Energy Environ. Mater.* **2024**, *7*, E12514.
- [103] Z. P. Cai, C. Ma, X. Y. Kong, X. Y. Wu, K. X. Wang, J. S. Chen, *ACS Appl. Mater. Interfaces* **2022**, *14*, 57047.
- [104] W. Liu, J. Liu, Z. Yang, M. Liu, S. Sang, H. Liu, *Adv. Funct. Mater.* **2025**, *35*, 2419095.
- [105] M. H. Hossain, M. A. Chowdhury, N. Hossain, M. A. Islam, M. H. Mobarak, *Chem. Eng. J. Adv.* **2023**, *16*, 100569.
- [106] N. Mahne, B. Schafzahl, C. Leybold, M. Leybold, S. Grumm, A. Leitgeb, G. A. Strohmeier, M. Wilkening, O. Fontaine, D. Kramer, C. Slugovc, S. M. Borisov, S. A. Freunberger, *Nat. Energy* **2017**, *2*, 17036.
- [107] M. D. Tikekar, S. Choudhury, Z. Tu, L. A. Archer, *Nat. Energy* **2016**, *1*, 16114.
- [108] P. Sayavong, W. Zhang, S. T. Oyakhire, D. T. Boyle, Y. Chen, S. C. Kim, R. A. Vilá, S. E. Holmes, M. S. Kim, S. F. Bent, Z. Bao, Y. Cui, *J. Am. Chem. Soc.* **2023**, *145*, 12342.
- [109] B. Li, X. Zhang, T. Wang, Z. He, B. Lu, S. Liang, J. Zhou, *Nano-Micro Lett.* **2022**, *14*, 6.
- [110] H. He, L. Wang, M. Al-Abbas, C. Cao, H. Li, Z. Xu, S. Chen, W. Zhang, R. Li, Y. Lai, Y. Tang, M. Ge, *Energy Environ. Mater.* **2024**, *7*, E1269.
- [111] J. Shi, K. Jiang, Y. Fan, L. Zhao, Z. Cheng, P. Yu, J. Peng, M. Wan, *Molecules* **2024**, *29*, 3624.
- [112] Y. Shi, W. Ye, D. Hua, Q. Zhou, Z. Huang, Y. Liu, S. Li, T. Guo, Y. Chen, S. J. Eder, H. Wang, *Mater. Today Phys.* **2023**, *38*, 101220.
- [113] L. Zheng, R. Lv, C. Luo, Y. Guo, M. Yang, K. Hu, K. Wang, L. Li, F. Wu, R. Chen, *Adv. Energy Mater.* **2024**, *14*, 240202.

- [114] C. Xu, T. Zhao, K. Wang, T. Yu, W. Tang, L. Li, F. Wu, R. Chen, *Adv. Funct. Mater.* **2025**, *33*, 2425487.
- [115] H. Wang, Y. Yuan, Q. Jia, A. Shao, M. Zhang, Z. Wang, L. Cheng, X. Tang, S. Li, Y. Ma, *Adv. Funct. Mater.* **2024**, *34*, 2314186.
- [116] L. Cheng, J. Liu, Y. Wang, H. Wang, A. Shao, C. Li, Z. Wang, Y. Zhang, Y. Li, J. Tang, Y. Guo, T. Liu, X. Zhao, Y. Ma, *Adv. Mater.* **2025**, *37*, 2420255.
- [117] J. Ge, C. Ma, Y. Zhang, P. Ma, J. Zhang, Z. Xie, L. Wen, G. Tang, Q. Wang, W. Li, X. Guo, Y. Guo, E. Zhang, Y. Zhang, L. Zhao, W. Chen, *Adv. Mater.* **2024**, *40*, 2413253.
- [118] D. Cao, X. Sun, Q. Li, A. Natan, P. Xiang, H. Zhu, *Matter.* **2020**, *3*, 57.
- [119] A. Sarkar, L. Velasco, D. Wang, Q. Wang, G. Talasila, L. De Biasi, C. Kübel, T. Brezesinski, S. S. Bhattacharya, H. Hahn, B. Breitung, *Nat. Commun.* **2018**, *9*, 3400.
- [120] D. Wang, S. Jiang, C. Duan, J. Mao, Y. Dong, K. Dong, Z. Wang, S. Luo, Y. Liu, X. Qi, *J. Alloys Compd.* **2020**, *844*, 156158.
- [121] H. Chen, N. Qiu, B. Wu, Z. Yang, S. Sun, Y. Wang, *RSC Adv.* **2020**, *10*, 9736.
- [122] K. Wang, W. Hua, X. Huang, D. Stenzel, J. Wang, Z. Ding, Y. Cui, Q. Wang, H. Ehrenberg, B. Breitung, C. Kübel, X. Mu, *Nat. Commun.* **2023**, *14*, 1487.
- [123] J. Yan, D. Wang, X. Zhang, J. Li, Q. Du, X. Liu, J. Zhang, X. Qi, *J. Mater. Sci.* **2020**, *55*, 6942.
- [124] L. Li, M. Hua, J. Li, P. Zhang, Y. Nie, P. Wang, X. Lin, Z. Zhang, R. Wang, X. Ge, Y. C. Li, L. Yin, *ACS Nano.* **2025**, *19*, 4391.
- [125] X. Li, G. Zhang, D. Zhang, R. Yang, H. Yu, X. Zhang, G. Lian, H. Hou, Z. Guo, C. Hou, X. Yang, F. Dang, *Energy Environ. Sci.* **2024**, *17*, 8198.
- [126] X. Cao, K. Fang, M. Cui, Y. Zhang, S. Li, X. Zheng, R. Yang, *Appl. Surf. Sci.* **2025**, *682*, 161660.
- [127] X. Li, Z. Qiang, G. Han, S. Guan, Y. Zhao, S. Lou, Y. Zhu, *Nano-Micro Lett.* **2024**, *16*, 55.
- [128] J. Mi, X. Chen, Y. Ding, L. Zhang, J. Ma, H. Kang, X. Wu, Y. Liu, J. Chen, Z. S. Wu, *Chin. J. Catal.* **2023**, *48*, 235.
- [129] H. Guan, Z. Cai, X. Wu, K. Wang, J. Chen, *Angew. Chem. Int. Ed.* **2025**, *35*, e202509132.

Manuscript received: July 28, 2025

Revised manuscript received: September 15, 2025

Version of record online: